Oxide-Metal Nanoparticles using Laser Ablation of Microparticle Aerosols

by

Manuj Nahar

Thesis

Presented to the Faculty of the Graduate School of

The University of Texas at Austin

in Partial Fulfillment

of the Requirements

for the Degree of

Master of Science in Engineering

The University of Texas at Austin

August 2009

Oxide-Metal Nanoparticles using Laser Ablation of Microparticle Aerosols

Approved by
Supervising Committee:

_____

(Desiderio Kovar)

_____

(Miachel Becker)

Dedicated to Dr. Vijay K Vasudevan

Acknowledgements

This work would not have appeared in its present form without the assistance, knowledge and patience of several individuals and organizations. I am deeply indebted to the members of the faculty, fellow graduate students, friends and family for their support.

First and foremost, I would like to express my deep and sincere gratitude to my advisor, Dr. Desiderio Kovar, for his time, guidance and patience. I would also like to thank Dr. John Keto and Dr. Miachel Becker for their time, sharp lecturing and guidance. I cannot possibly thank Ignacio Gallardo enough for his help. Special thanks to Hoda Tavakoli, Kris Gleason, Nathan Erickson, Dr. Arindam Sarkar and Ganesh Iyyer. Many thanks to Dr. Lew Rabenberg, Dr. J.P. Zhou, Michael Ronalter, Dr. Benny Freeman, Dr. Graham Henkelmen and Dr. Manthiram for their very useful advice and discussions.

I would also like to thank the friends that I met in Austin – Achint Aggarwal, Akshara Richarya, Anuj Arora, Carl Seimen, Chetan Sandhu, Daniel Carney, Dhruv Mohta, Illiana Marine Lopez, Sohaib Alam, Nishesh Mehta, Anirudh Mohtnot, Vijo Varkey, Monica, Allen, Matthew Garza, Luke Duffey, James, Zach, Miachel Asoro, Meagan Wooley, Melissa Rodriguez, Simon, Robert Morgan and many others.

My family and friends back home – Ma, dad, dada, dadi, and Garima who supported me and believed in me, and forgave me for not being with them when they wanted my support.

Abstract

Oxide-Metal Nanoparticles using Laser Ablation of Microparticle Aerosols

Manuj Nahar, M.S.E.

The University of Texas at Austin, 2009

Supervisor: Desiderio Kovar

We have studied a continuous aerosol process for producing oxide nanoparticles with sizes of 10-60 nm that are decorated with smaller 1-3 nm metallic nanoparticles. Such particles may be useful in a number of areas including catalysis and as contrast enhancement agents in biomarkers. To produce the oxide nanoparticle carriers, an aerosol of 1-10 µm oxide particles are ablated using an excimer laser. The resulting oxide nanoparticle aerosol is then mixed with 1-2 µm metallic particles and this mixed aerosol is ablated a second time. The oxide nanoparticles are too small to ablate but act as seeds for the nucleation of metallic nanoparticles on the surface of the oxide. The nanoparticle sizes can be varied by changing the gas type or gas pressure in the aerosol. We

demonstrate the feasibility of such an approach using two oxides, SiO_2 and TiO_2, and two metals, Au and Ag.

Table of Contents

List of Figures

Chapter 1: Introduction

Section 1.1: Motivation for NP Research

Developments in physical chemistry, microscopy, biochemistry, device physics and engineering have resulted in a tremendous upsurge of interest in the properties and preparation of nanostructures and their possible applications in a wide variety of areas. At the nanometer scale, the physical, chemical, and biological properties of materials differ in fundamental and valuable ways from the properties of individual atoms and molecules or bulk matter. For example: bulk gold is inert, whereas nano-sized gold particles act as a catalyst for various chemical reactions [1]. Furthermore, it is possible to change the principal parameters (such as their morphology, shape etc.) of nanostructures to fine tune the desired engineering properties. Technological innovations have enabled the manipulation of various nanostructures such as quantum dots, nanoshells, nanotubes, nanorods, nano-tetrapods, nanospheres and others. In the present work we explore the possibility of fabricating unique, two-phase nanoparticles such as island particles using a physical approach and determine the processing parameters that control the morphology of such particles.

1.1.1 Selected Properties of NPs

The principal parameters that define NPs are their shape, aspect ratio, size, morphological sub-structure and the chemical and physical environment around them. These principal parameters determine the physical and chemical properties of a NP.

Surface Area (SA) to Volume (V) Ratio: The significance of SA/V stems from the fact that most chemical reactions take place at the surface of a material. For a spherical particle, volume is given by $4/3\pi r^3$, while the surface area is given by $4\pi r^2$ (where r is the particle radius). The ratio SA/V is thus inversely proportional to r and increases tremendously as we approach the nanoscale regime. Reaction kinetics are thus greatly enhanced by an increased SA/V ratio. This increased reactivity for higher surface area to volume ratio is widely taken advantage of in the design of catalysts [2].

Quantum Confinement Effects: The size of very small NPs (~ 1-2 nm) is comparable to the wavelength of an electron wave function. When the dimensionality of a material becomes so small, then the electron energy levels can no longer be treated as continuous, meaning that there is a small and finite separation between energy levels. This situation of discrete energy levels is called quantum confinement [3]. Under these conditions, the behavior of a semiconductor material ceases to resemble bulk, and instead is referred to as a

quantum dot. Electrons trapped in these quantum dots behave like a particle in a box. The discrete energy levels also induce a significant size dependence [4] on quantum dots; addition and subtraction of a few atoms can change the properties remarkably. A shape dependence [5] on quantum confinement effects has also been recently observed.

Optical Properties: Like many other characteristics of NPs, interactions with electromagnetic radiation depend on the size of the particles [6]. The optical spectrum of several systems has been observed to change strongly by reducing their size. This change has also been attributed to quantum confinement which introduces extra localization energy and changes the density of states. There is a significant shift in the absorption spectra towards the blue (shorter wavelength) as the particle size is reduced. For example: A shift in the absorption spectra and emission spectra of several materials including gold and silica, have been observed on changing their size. Optical properties of these systems with reduced size, thus allows one to fabricate tailor-made materials for novel optical components. The optical properties of NPs can be utilized for molecular sensing [7], diagnostic [8] and imaging applications [9].

Electronic and Magnetic Properties: Materials with metallic, semiconducting and insulating characteristics in bulk have shown interesting electrical properties at the

nanoscale [10]. As with bulk semiconductor materials, electrons in nanoscale materials tend to exhibit transitions near the edges of the bandgap. However, with quantum dots, the size of the bandgap is controlled simply by adjusting the size of the dot. Metallic NPs self assembled on specific solid substrates have shown increased conductivity [11]. Insulating materials such as ZnO [12], have been shown to exhibit a semiconducting nature in the nano size regime. The size dependence of electrical properties of nanomaterials is largely exploited in the design of semiconductor devices.

Small NPs also exhibit unique magnetic properties i.e. the particles do not retain their magnetization due to the lack of domains (i.e. supermagnetic). For example: several ferromagnetic materials become supermagnetic below 20 nm [13]. The interaction of electromagnetic pulses with such NPs can be used for enhanced drug delivery in solid tumors [14].

Section 1.2 Methods of Producing NPs

Various chemical, physical, biological, self-assembly and hybrid methods for the production of NPs have been developed. A few commonly used methods have been outlined here:

Wet Chemical Synthesis: [15,16]

Condensed phase NP synthesis methods were developed with the goal of controlling the size, crystallinity, and dispersity of the particles precisely. Early work concentrated on simple solution phase synthesis, while recently more complicated materials and preparation of self-assembled nanostructures are being explored. A few condensed-phase preparation methods are listed below.

(a) Homogenous precipitation methods [17]: Isolated nanoclusters can be precipitated from a crystalline or amorphous matrix of the material dissolved in the appropriate solvent. If the matrix can be dissolved selectively without dissolving the clusters, a colloidal suspension of nanoclusters can also be obtained. Metallic nanoclusters can be prepared by the addition of a reducing agent to an acidic solution of metal ions. Organic solvents can also be used to prepare colloidal suspensions, where the size of NPs is controlled by strongly bonded solvent molecules.

b) Sol-gel Method [18]: The sol-gel method is a chemical technique that uses metal alkoxides for synthesis and production of glasses or ceramics using various chemical processes, including hydrolysis, gelation, drying and thermal treatment. In general, a sol is defines as a colloid of solid particles suspended in a liquid, while a gel is a composite substance consisting of continuous solid skeletal structure, which results from the gelation of the sol. The gel forms a cell that

encapsulated the colloidal liquid. The solute can be driven from the gel through a thermal treatment, and solid glass or ceramic NPs are thus produced.

(c) Microemulsions: Microemulsions are clear, stable, isotropic liquid mixtures of oil, water and surfactant. These microemulsions can be prepared spontaneously by maintaining very low interfacial tension and by the addition of a co-surfactant. The surfactant molecules help prevent unwanted particle growth and protect the NPs from oxidation, providing the necessary passivation to the NPs. Various metallic, semiconductors, superconducting and magnetic NPs are prepared via this technique [19].

(d) Combustion or Propellant Synthesis [20]: Combustion synthesis is a popular method to produce gram quantities of phosphor materials. An aqueous precursor solution containing metal salts, typically nitrated that serve as the oxidizer, and fuel such as glycine is heated slowly in a furnace to evaporate water until rapid combustion occurs. The explosive nature of reaction results in formation of NPs with no subsequent particle growth. The particle size depends on the reaction temperature, which is controlled by adjusting the fuel-to-oxidizer ratio.

Physical Methods

(1) Gas Aggregation of Monomers: This method establishes a monomer population by evaporation, either using an oven source or by laser ablation [21]. Subsequent cooling of monomers and growth of clusters/particles by successive addition of monomers, results NPs.

(2) Mechanical Attrition/ Ball Milling [22]: In this method the grain size of powder materials is reduced to the nano level by mechanical deformation. Pure bcc metals (eg: Cr, Nb), hcp metals (eg: Hf, Zr) and compounds (eg: FeAl) can be ball milled to produce their NPs. Several catalytic [23] and magnetic materials [24] are produced by this process.

(3) Pulse Laser Deposition [25]: This technique is a physical vapor deposition technique, where a high power laser is used to vaporize a target material, which later deposits on a substrate as a thin NPs film. The electric field generated from the laser light removes the electrons for the target material, which oscillate within the electromagnetic field of the laser, colliding with the atoms of the bulk materials and vaporizing them during the process. The vaporized atoms are deposited on a substrate, in the form of a thin film. This laser irradiation can be carried out in ultra high vacuum or in the presence of a buffer gas such as oxygen, to deposit oxide NPs of the material. It should be noted that the ablation process reported in our work is significantly different from the one described in this work.

(4) Vacuum Sputtering [26]: In this method a target material is bombarded with inert gas ions and the sputtered atoms are collected on a temperature controlled substrate. The method is frequently used to fabricate multi layered nanocomposite materials, metallic materials and insulating materials.

Self-Assembly Techniques

Self assembly techniques [27] assemble the NPs on a suitable substrate and link them in a certain manner. Self assembly techniques for the formation of NPs, are a two step process – 1) The synthesis of NPs (in many case in colloidal form), 2) Self assembly of the particles on a substrate. The NPs formed via a colloidal route can be capped with suitable surfactants, which might also aid in self assembly. The NPs molecules may bond with the surface of the substrate by hydrogen bonding, electrostatic interaction or covalent bonding.

Section 1.3 Multicomponent Nanostructures

Until recently, most inorganic nanomaterials synthesis was limited to single component form. Multicomponent composite nanostructures [28] have thus become the immediate research area to meet more challenging applications. A

multicomponent nanostructure can be defined as a material system of a solid compound of one material prepared on a support of another material. The support in these systems becomes an integral part of the final product and can substantially alters the physical and chemical properties. Wet chemical methods are the most common technique used to prepare these complex nanostructures. We will restrict our discussion to the synthesis of inorganic multicomponent systems. Presently, there are two common methods to produce such structures – (1) surfactant-assisted organization [29], where the surfactant acts as a linkage between the two components of the structure, and (2) patterned substrate deposition, which utilizes lithographic [30] and imprinting techniques. A few multicomponent nanostructures and techniques to generate such structures, with special emphasis on core-shell NPs are discussed below. Each of these approaches has their own advantages and disadvantages, which will be discussed later.

Clusters of Gold NPs on Functionalized Silica NPs

Halas *et al*. reported the preparation of small gold nanoclusters on the surfactant of functionalized silica NPs [31]. Gold NPs diluted in water and ethanol led to the self assembly of gold NPs in aggregates of regular shapes and sizes. Functionalization of the surfaces of silica NPs with different terminal groups influenced the coverage of gold nanopclusters. Hydrophilic functional groups such as NH_2 and SH bound to the gold NPs, while hydrophobic functional groups such

as CH_3 and PPh_2 did not. The coverage of the gold NPs was thus controlled by the amount of dilution and the type of functional group used.

Core-shell NPs with silica shell

A silica shell over inorganic NPs provides several benefits such as oxidation resistance, stability against degradation and coagulation, and biocompatibility. Microemulsions are one of the common methods to produce such structures. For example: Silica-CdS core-shells were prepared via the simultaneous co-precipitation of CdS in water droplets during silica sphere synthesis via the hydrolysis of Tetraethyl Orthosilicate (TEOS) in microemulsions. Similarly Ag-silica core-shells were prepared via the *in-situ* photochemical reduction of Ag ions during the hydrolysis of TEOS in microemulsions [32]. Silica-coated magnetic particles have tremendous potential in biomedical engineering. Silica-coated iron oxide particles were prepared by the precipitation of iron oxides with NH_4OH in nonionic reverse micelles, followed by NH_4OH-catalyzed hydrolysis of TEOS [33]. Rod-like Fe_2O_3 - silica nanocomposites have also been synthesized using a similar approach. Other magnetic materials such as $CoFe_2O_4$ and $MnFe_2O_4$ core-shells have also been synthesized using a microemulsion technique.

CdSe/ZnS amd CdSe/CdS

CdSe/ZnS is the most studied core-shell structure. Its synthesis was first reported by Hines and Guyot-Sionnest, who prepared a ZnS overcoat on 3 nm CdSe cores [34]. A mixture of the organometallic precursors diethylzinc and hexamethyldisilathiane, $S(TMS)_2$, at high temperature (300 ^oC), was used to form ZnS shell. A similar approach was later applied for forming ZnS – CdSe core-shell nanorods. The addition of hexadecylamine (HDA) to trioctylphosphine oxide/trioctylphosphine (TOPO/TOP) solvent system led to a better control of the growth kinetics during both the CdSe core and ZnS shell synthesis, resulting in a narrower size distribution and quantum yields (QYs) on the order of 60%. Recently, extremely small CdSe/ZnS core-shell nanocrystals have been synthesized by Kudera *et al* [35]. The ZnS shell in the core-sell structures discussed above provide an efficient confinement of electron-hole wave function and exhibit an enhanced photoluminescence efficiency [36].

Section 1.4 Gold Islands on Titania as a Catalyst

Although gold is a poor catalyst in the bulk form, the recent discovery of high catalytic activity of oxide-supported gold NPs has led to inspiration for exploring nanoscale gold catalysis [37], typically for CO oxidation reactions. The achievement of highly active catalysts has been shown to require gold particles less than 5 nm [38]. Partial electron transfer from the surface to the gold islands is believed to play an essential role in the catalytic activity of these systems. Also,

the decrease of mean surface coordination number and the ready mobility of Au atoms on the surface, could lead to greater chemisorptivity, a larger coverage of oxygen, and a stronger interaction with a support to create special gold sites near the support. The oxidation of CO is postulated to occur preferentially on the peripheral edges between gold NPs and oxide support [39]. However, the precise reason for the increased catalytic activity of gold particles in the restricted size range is not clear. The gold-tiania catalyst designed so far have a planar geometry. A core-shell structure of gold on titania would give a much higher surface to volume ratio and thus higher catalytic activity.

Section 1.5: Objectives of the Thesis

In this present work, we present a method to produce metal-on-oxide NPs via the Laser Ablation of Microparticles (LAM) in aerosol. The LAM process was developed at the University of Texas at Austin by Dr. J.W. Keto, Dr. M.F. Becker and Dr. J.R. Brock [40]. The technique is capable of producing bare NPs of a variety of inorganic materials, with a relatively narrow size distribution. The process, essentially converts a microparticle aerosol to a NPs aerosol by generating a traveling shockwave in the microparticles, which vaporizes and condenses the microparticles to form NPs. The LAM process is further discussed

in the subsequent chapters. The process forms NPs of sizes 1-50 nm depending on the operating parameters.

Gold NPs on a titania substrate have proven to be candidates for a variety of catalytic reactions, and have other applications. Wet chemical synthesis methods, similar to the one discussed in section 1.2 have been employed previously to produce these particles. However, to exploit the catalytic properties of the gold-titania system and to realize its true physical and chemical properties, it is necessary to establish effective means to remove the organic shell that occurs inevitably as a byproduct of chemical synthesis methods. The LAM process is ideally suited for producing bare NPs. A modified double step LAM process was explored to fabricate these multicomponent nanostructures in our work.

We first describe the synthesis techniques used to synthesize our feedstock microparticles for the process. The feasibility of our process to produce metal-on-oxide NPs is established using two metals and two oxides. The NPs are characterized using a JEOL 2010F Transmission Electron Microscope (TEM). The effect of process parameters (gas atmosphere and laser fluence) on particle size distribution is discussed. We employed two different routes to form our NPs and discuss the pros and cons on each. The potential use of gold on titania NPs as catalysts depends on their size stability at high temperatures. Gold NPs have been previously shown to sinter into larger particles at higher temperatures, reducing the catalytic activity substantially [41]. Preliminary heating experiments to

investigate the stability of NPs using the electron beam of the TEM were thus performed on the NPs.

Chapter 2: The Laser Ablation of Microparticle (LAM) Aerosol Process

Section 2.1: Laser Ablation of a Microparticle: Shockwave Generation Process

The laser ablation process for a single microparticle [42] is shown schematically in Figure 2.1.1. A laser fluence above the breakdown threshold of the particle results in plasma breakdown and the generation of a shockwave. Breakdown occurs at the front edge of metallic particles and near the rear edge of dielectric particles. This shockwave compresses and heats the particle above the critical point. Condensation of NPs occurs in the low pressure region behind the shockwave, as expansion and cooling occurs. The expansion of the heated material is determined by the gas atmosphere and pressure, which determines the rate of coalescence of the vapor and thus the NP size. NPs formed by the LAM process have been shown to have mean diameters ranging from 1-50 nm. Thermionic emission and photo ionization occurs during the process, imparting the particles with a positive charge. The positively charged NPs repel each other [43], preventing agglomeration, and ensuring a concentrated NP aerosol. However, recombination of these charged particles with free electrons occurs with time, resulting in agglomeration of NPs, if they are not collected quickly.

Stage 1. Initial Breakdown

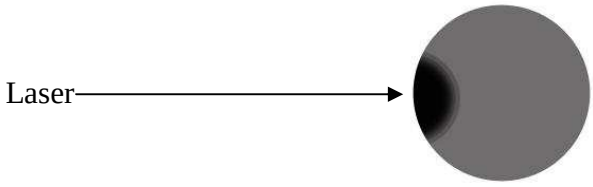

The laser pulse is absorbed at the front surface of metal particles.

Stage 2: Shockwave Formation

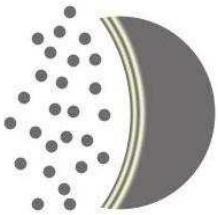

Laser-induced breakdown occurs at the front surface producing a shockwave, which travels through the particles.

Stage 3: Nucleation, Coalescence and Particle Charging

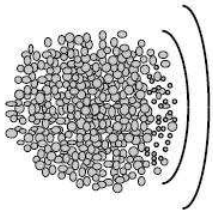

The vapor is rapidly quenched in the low pressure region behind the shockwave. The particles condense and are charged due to thermionic emission and photo ionization.

Figure 2.1.1 (a): Laser ablation of a metal microparticle (redrawn from "Nanoparticle Produced via Laser Ablation" [44]).

Stage 1. Initial Breakdown

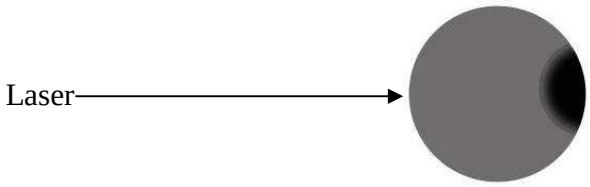

The laser pulse is absorbed at the rear surface of dielectric particles.

Stage 2: Shockwave Formation

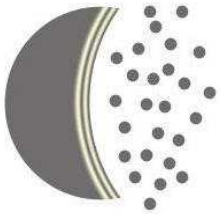

Laser-induced breakdown occurs at the rear surface producing a shockwave, which travels through the particles.

Stage 3: Nucleation, Coalescence and Particle Charging

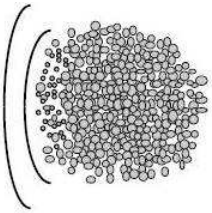

The vapor is rapidly quenched in the low pressure region behind the shockwave. The particles condense and are charged due to thermionic emission and photo ionization.

Figure 2.1.1 (b) : Laser Ablation of a dielectric microparticle (redrawn from "Nanoparticle Produced via Laser Ablation" [44]) .

Section 2.2: Laser and Optical Setup

A Lumonics KrF excimer laser is used for our LAM setup. The laser is filled with a KrF/Ne gas mixture to produce 200 Hz, 10 ns laser pulses at a wavelength of 248 nm. The laser produces a maximum peak output of ~ 650 mJ and can be efficiently used for long durations at an output of 350 mJ. The laser is first directed into a cylindrical lens with a focal length of 120 cm, which focuses the height of the beam. The beam is then directed through another lens with a shorter focal length of 24 cm. The shorter focal length lens can be positioned to achieve the desired laser fluence in the first or second ablation region. The lenses can be adjusted using fine thumb screws to precisely align the laser beam. The resulting beam has dimensions 4 mm by 2 mm at the ablation spots.

Section 2.3: Aerosol Feeder

A high density microparticle aerosol is required to maximize NP output. The aerosol generator shown in the Figure 2.3.1 was used to aerosolize the feedstock microparticles. It consists of a stainless steel, hollow cylinder (ID = 2.13 cm, OD = 3.75 cm and height = 4.40 cm), fitted to a detachable transparent plastic lid with o-ring seals and four screws. The bottom of the cylinder has a flexible rubber membrane, which is in contact with a thin steel mesh support. An iron plunger sits

below this steel mesh. A fairly stiff spring is attached to the plunger. A vibrating solenoid driven at a frequency of 1−10 Hz is used to drive the iron plunger-spring system, which in turn impacts the rubber membrane. Each impact on the membrane shoots the microparticles in the drum feeder high enough to be picked up by the carrier gas. The carrier gas enters and exits the drum feeder through a 0.63 cm tube. The amount of powder that enters the ablation cell depends on three factors – (1) The amount of powder inside the cylindrical drum, (2) The flow rate of the carrier gas, (3) The frequency of the solenoid. The frequency of the individual feeders and the amount of powder in each feeder can thus be adjusted to control the amount of oxide or metal feedstock particles as required. The drum feeders used can be used to aerosolize a small quantity of powder only.

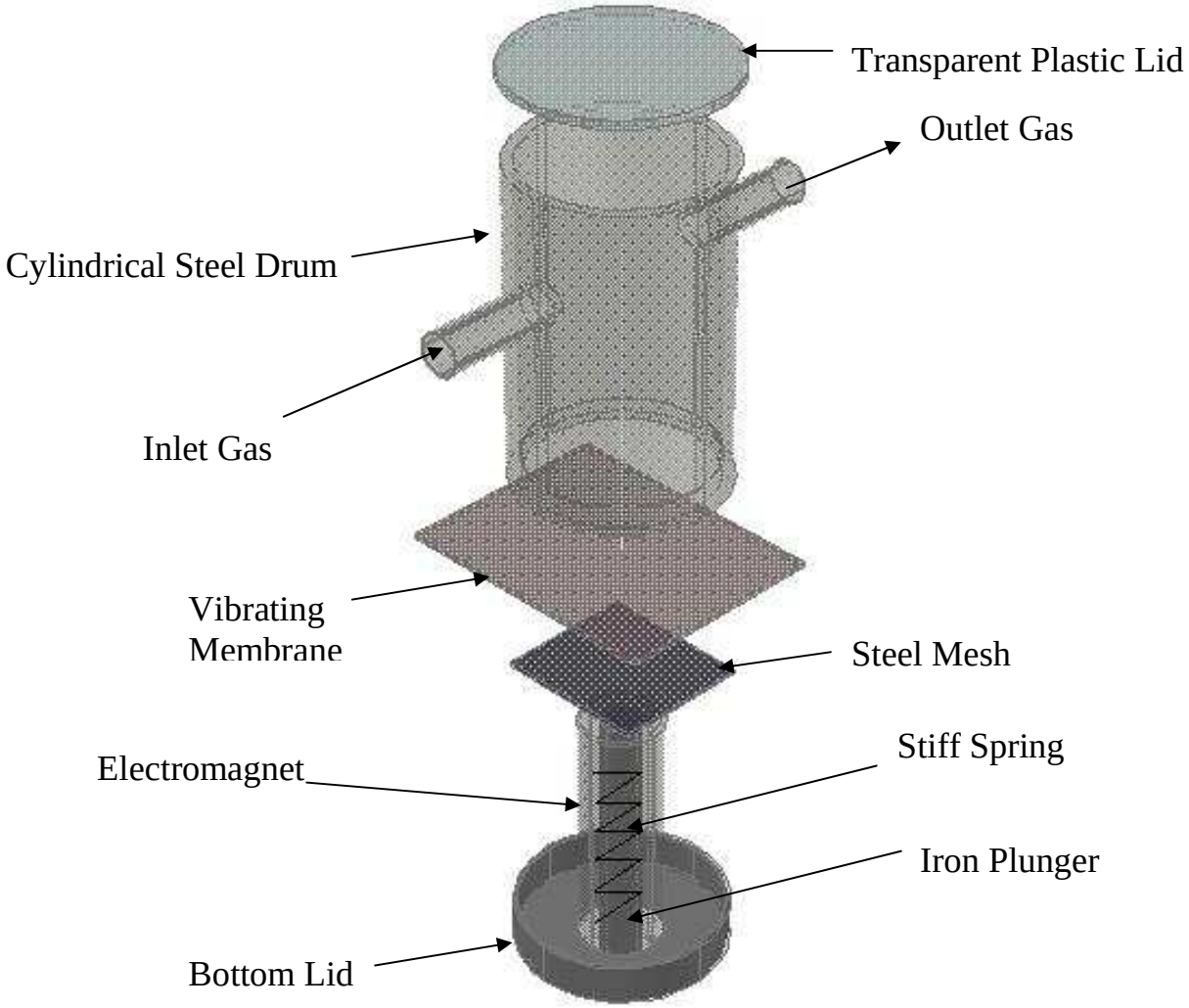

Figure 2.3.1: Aerosol Generator.

Section 2.4 The Double Ablation Chamber

The ablation chamber shown in Figure 2.4.1 was fabricated out of borosilicate glass in the glass shop at The University of Texas at Austin, by Mr. Miachel

Ronalter. It is made of two crosses of glass tubes of internal and outer diameter 1.63 cm and 1.90 cm respectively. The long axis (laser beam axis) of the chamber is 6.23 cm long and length of the glass tubes on the perpendicular axis (aerosol flow axis) is ____ cm long. At one of the ends on the long axis a funnel is attached with a rubber fitting. The larger opening of the funnel can be attached to an MgF-coated (antireflection material), quartz window. The MgF coating on long exposure to high laser fluences gets solarized, if it is coated with particles and thus must be cleaned regularly and replaced whenever necessary. The other end of the long axis is fitted to a quartz tube, and can sustain direct laser exposure. The quartz tube is covered with aluminum foil to dissipate heat and protect the quartz. Small cylindrical steel fittings with nozzles are attached to the other three openings of the cross, while the fourth opening is fitted to another steel attachment which facilitates the insertion of the electrostatic NP collection system and also serves as a vent for vacuum. The steel fittings with nozzles have separate inlets for both the center and coaxial gas flow. The main flow and coaxial flow are controlled by separate manual valves and separate flowmeters (graduated in L/min). The gas cylinders for the carrier gas are maintained at a pressure less than 103 KPa. The coaxial flow and center flow are introduced before the gas enters the first ablation chamber and the second ablation chamber. The coaxial flow is essential to laminarize the microparticle flow, to ensure the ablation of most microparticles and collection of all NPs. Also a turbulent flow might lead to the

deposition of NPs on the front window, degrading the MgF coating. The coaxial gas is exhausted to vacuum at the end of the first ablation region and is introduced again before the gas enters the second ablation region. A metal aperture is introduced in the first ablation region, also to ensure a laminar flow. The laser beam, when properly focused, does not touch any part inside the chamber except the quartz tube at the chamber end. Laser alignment in this double LAM setup is particularly difficult to achieve, but is possible due to the visible ablation of the metal aperture, or other parts of the chamber. The entire chamber is held in place using three clamps, giving it the desired flexibility for alignment. However, the present setup suffers from two major drawbacks – 1) The collection distance for the oxide NPs is long and thus oxide NPs may agglomerate due to recombination, 2) The fluence on NPs is limited, which may result in a broad size distribution.

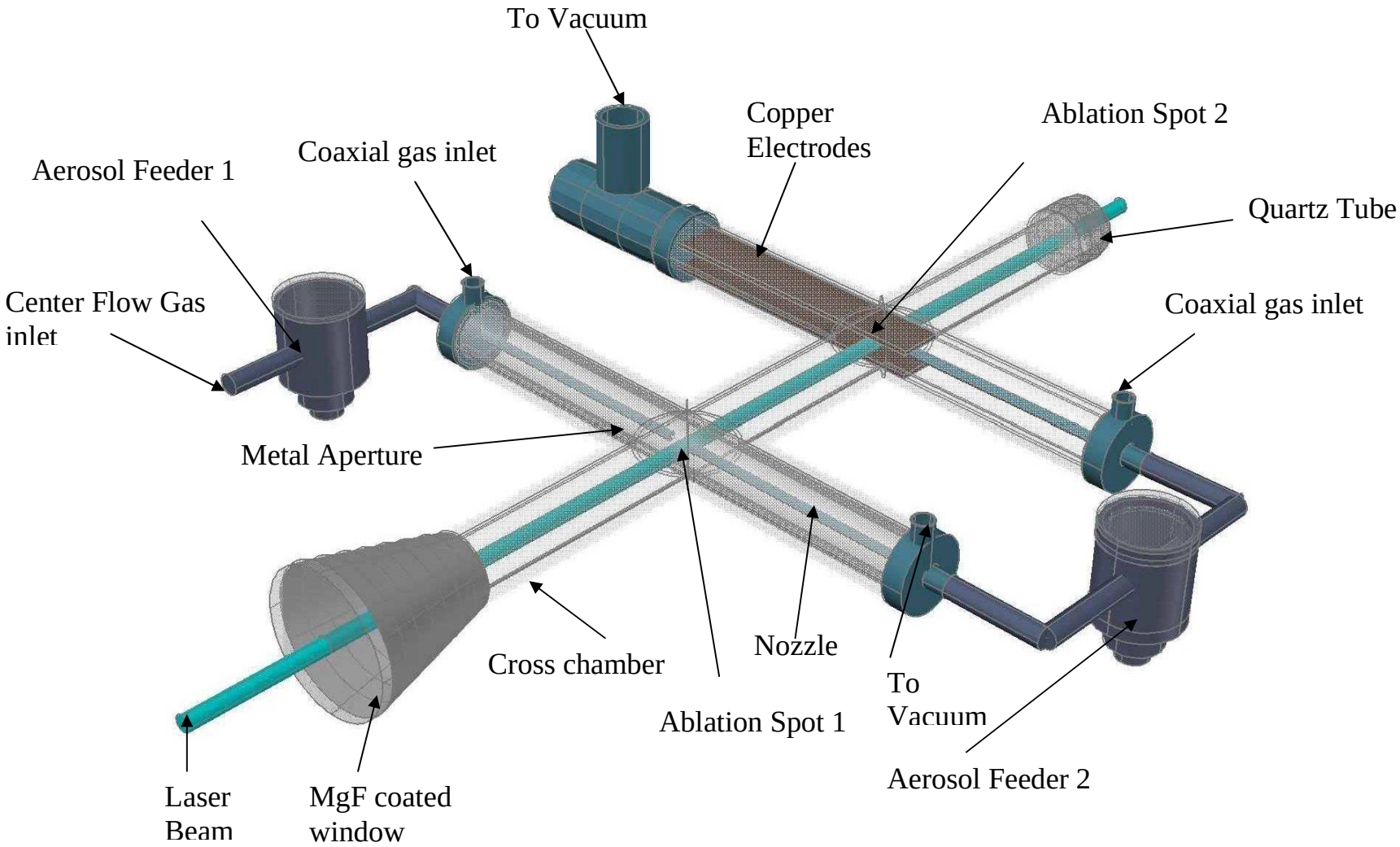

Figure 2.4.1: Schematic of the double step LAM chamber.

Section 2.5 Electrostatic Collection

The NPs produced during the LAM process have a positive charge due to photoemission and thermionic emission. These charged NPs can thus be collected electrostatically by applying an electric field perpendicular to the trajectory of the NP aerosol. Two copper electrodes with a separation of 12 mm, as shown in Figure 2.5.1, are kept parallel to the main flow in the second ablation region. A potential difference of 500 V is applied to the electrodes. A charged NP experiences the drag force, the gravitational force and the electrostatic force when moving across this potential difference. The effect of these forces on the trajectory of NPs has been calculated by Henneke and the final equations are presented here [44]:

$$\vec{r} = \left\langle \frac{K_2}{(K_1)^2}\left(K_1 t + e^{-K_1 t} - 1\right), 0, \frac{K_3}{(K_1)^2}\left(K_1 t + e^{-K_1 t} - 1\right) \right\rangle$$

Equation (1)

It should however be noted that these equations are valid only for non-agglomerated particles and the NPs produced in the present work are often agglomerated. Also, these equations are valid only for a laminar flow. One of the advantages of the electrostatic collection system is its ability to size select between NPs and microparticles. Microparticles, owing to their higher momentum in the gas flow, are not significantly deflected by the electrostatic force while the NPs

are deflected and collected on the electrodes. The electrostatic collection can thus be used to collect these NPs on a substrate.

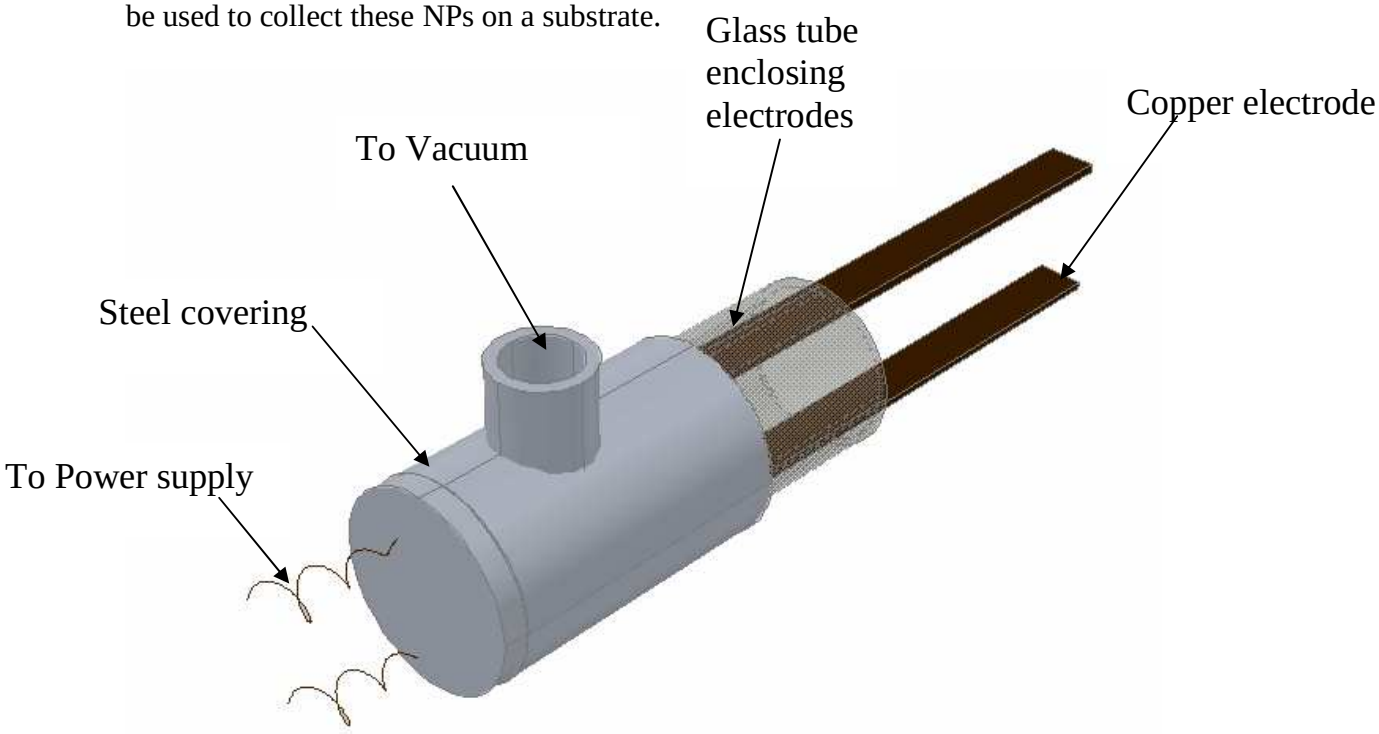

Figure 2.5.1: Schematic of electrostatic collection system.

Section 2.6: The Double Step LAM Process

The LAMA process for producing single component NPs [43] has been previously reported. For this study, an additional ablation step, shown schematically in Figure 2.6.1, was utilized to produce metal NPs on oxide NPs. Aerosolized feedstock particles are introduced to the ablation chamber in a carrier gas. The carrier gas consists of a coaxial gas surrounding the center flow to ensure a laminar flow of the aerosol through the ablation points. The main flow gas

carries the aerosolized oxide microparticles to Ablation point 1, where they are irradiated by the laser. The oxide microparticle aerosol is converted to a NP aerosol and mixed with metal microparticles in the second aerosol generator. The gas flow carried the mixed oxide NP/metal microparticle aerosol to Ablation spot 2. Because the absorption depth for the laser is larger than the oxide NPs, the oxide NPs are heated but do not reach the threshold for breakdown. As a result, the oxide NPs are reduced slightly in size by evaporation but otherwise remain intact. In contrast, a shockwave is generated in the larger metal microparticles that results in the formation of metal NPs that nucleate on the surfaces of the oxide NPs. The NPs formed are photo/thermally ionized and are collected electrostatically onto lacey carbon TEM grids.

It should be noted that double step LAM process is essential to fabricate core-shell like structures and such structures cannot likely be obtained by simply mixing the microparticles of the core and shell and ablating them simultaneously. A single step ablation of mixed microparticles would likely result in alloyed particles of the mixed materials [45]. The cooling rates in the process are extremely fast and even systems which do not form solid solutions readily are likely to alloy at such high cooling rates. Thus, to produce such multicomponent structures it is essential to have the core material in nano form at the ablation spot 2, so that the metal NPs can nucleate on the core NPs. Another approach would be to mix NPs of the core and microparticles of the shell and use single ablation to

produce particle-on-particle systems. However, NPs in powder form of most materials tend to agglomerate severely at room temperature and thus the double step ablation process is the only viable method to produce core-shell NPs.

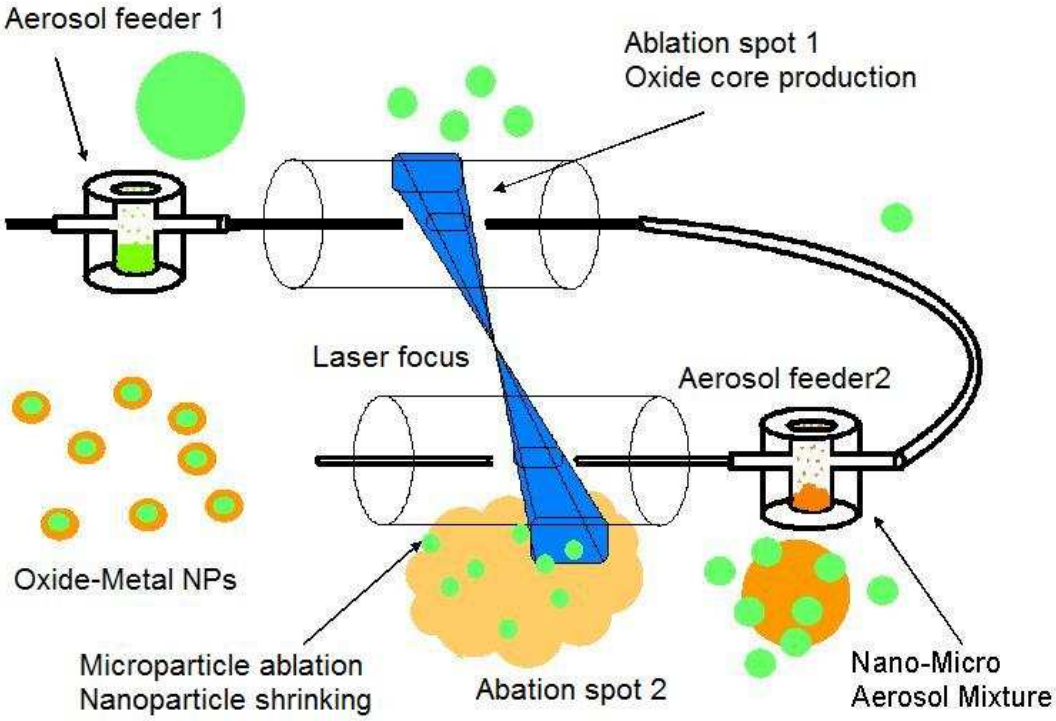

Figure 2.6.1 Schematic of the double step LAM process.

Section 2.7: An Alternative Approach

An alternative approach to produce metal on oxide particles was also evaluated in our work. This approach allowed the oxide microparticles to travel along the long axis of the chamber, instead of going through the second feeder. This is accomplished by disturbing the laminar flow of the oxide particles, so that the oxide NPs are exposed to the laser multiple number of times. Also, the oxide NP aerosol and metal microparticle aerosol, turbulently mix with each another at ablation spot 2. This alternative approach is an attempt to address the problem of agglomeration of the oxide NPs. However, the multiple ablations of oxide microparticles makes this approach uncontrollable, since the size of the oxide NPs depends on the number of ablations each particle experiences and it varies from NP-to-NP in this approach.

Chapter 3: Characterization of NPs and Microparticles

A JEOL 2010F TEM and a JEOL JSM-5610 Scanning Electron Microscope (SEM) were used to characterize the NPs and feedstock microparticles respectively. The particle sizes were calculated using Image J 1.41o [46].

Section 3.1: TEM Operating Conditions

Phase contrast analysis was used to characterize the NPs using a JEOL 2010F TEM. Typical TEM operating conditions were an acceleration voltage of 200 kV, no objective aperture and a condenser aperture of 70 microns. An Oxford INCA Energy Dispersive Spectrometer (EDS) attached to the microscope was used for quantitative phase analysis of the NPs.

Section 3.2: Image Processing and Particle Size Calculation Process

Image J 1.41o was used to process the phase contrast images and calculate the particle sizes. An automated particle counting process was used for calculating the size distribution of the feedstock microparticles, while a manual particle counting process was used for the NPs.

Image Processing and Particle Size Calculation Method for Microparticles: An example of feedstock silica microparticles is used to illustrate the image processing and particle counting steps for microparticles.

Initial Image: Figure 3.2.1 shows the SEM micrograph of the silica microparticles.

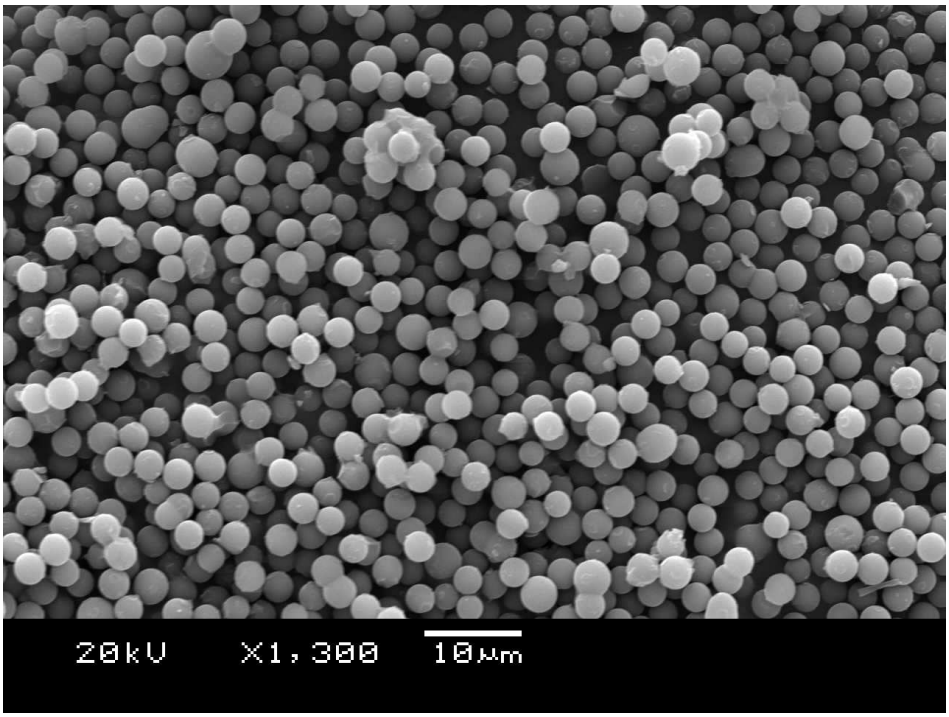

Figure 3.2.1: SEM micrograph of silica microparticles.

Step 1: The image is first converted to a binary image and the slightly overlapping particles are then separated using the Watershed tool, resulting in an image as shown in Figure 3.2.2.

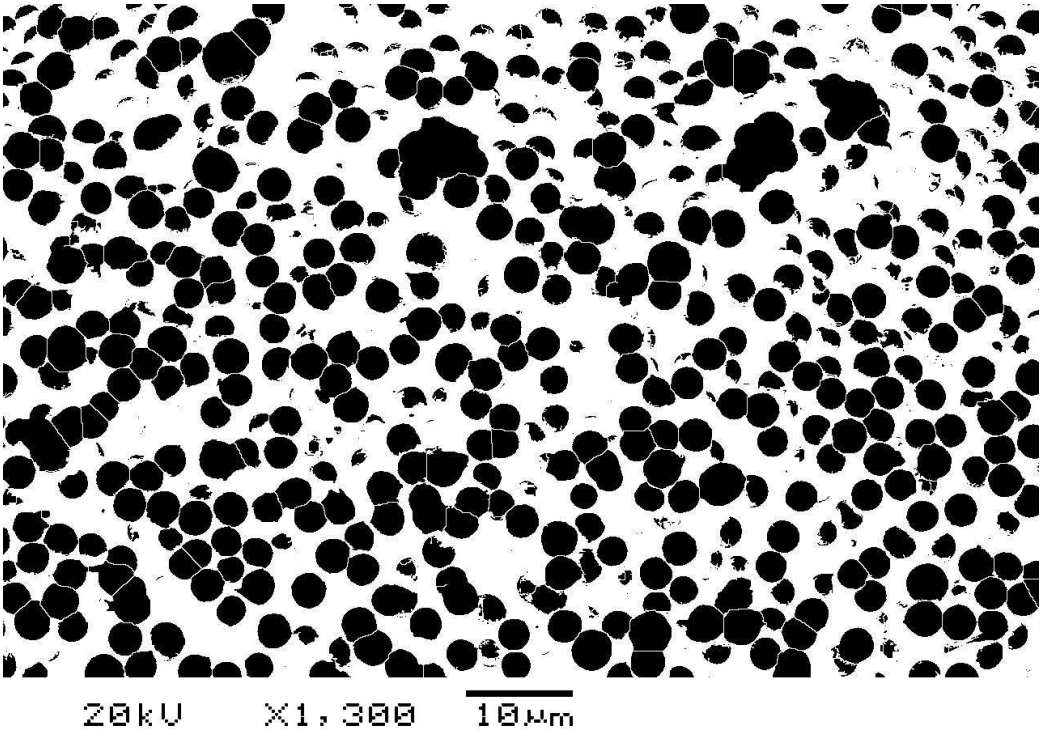

Figure 3.2.2: Silica microparticles image after being converted to a binary format and applying watershed operation.

Step 3: The Analyze Particles tool in Image J is then used to calculate the particle count and area of particles of a specified particle area and circularity range. It is evident that the smallest particle in the image is larger than 2 µm and the biggest particle is smaller than 4 µm. The circularity of particles is approximately between 0.8-1. We feed the above ranges of particle size and circularity in the program and count only those particles that belong to the specified range. An output image showing the particles counted by the program is generated and is shown in Figure 3.2.3. It should be noted, by accounting for the minimum and maximum particle

size and the circularity of the particles, we ensure only individual particles are counted by the Image J 1.141o program and the agglomerates and overlapping particles (which cannot be separated by the Watershed tool) are eliminated from the counting process. Assuming every particle to be a perfect sphere, we calculate the particle sizes from the given particle area.

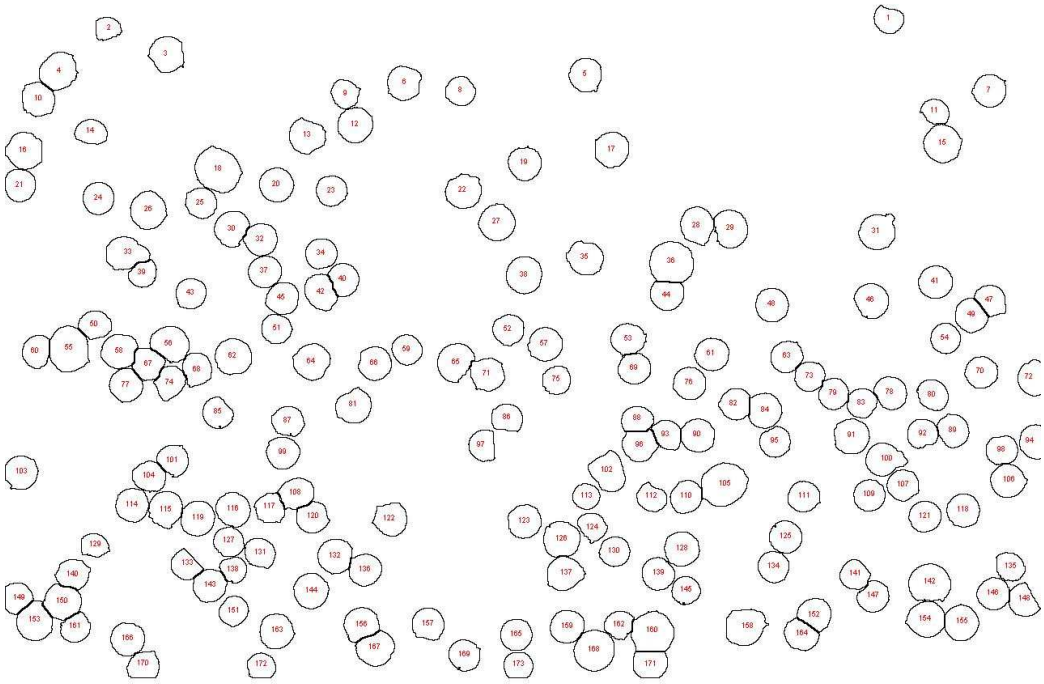

Figure 3.2.3: Image of particles counted by the Image J 1.141o program.

Image Processing and Particle Size Calculation Method for NPs: The above mentioned method for calculating particle size cannot be used for NPs, since a binary image of the TEM micrographs of NPs cannot distinguish between the

oxide NPs and metal NPs. However, as shown in Figure 3.2.4, contrast differences between the metal NPs (which appear to be darker) and oxide NPs (which appear to be lighter), allows one to manually distinguish between the oxide and metal NPs. The particle area is thus calculated manually by using the *Elliptical Selection* tool provided by Image J, which allows the user to draw a circle superimposing a NP and measuring its area and also counting the number of particles during the process. Particle size is then calculated from particle area, considering every particle to be a perfect sphere.

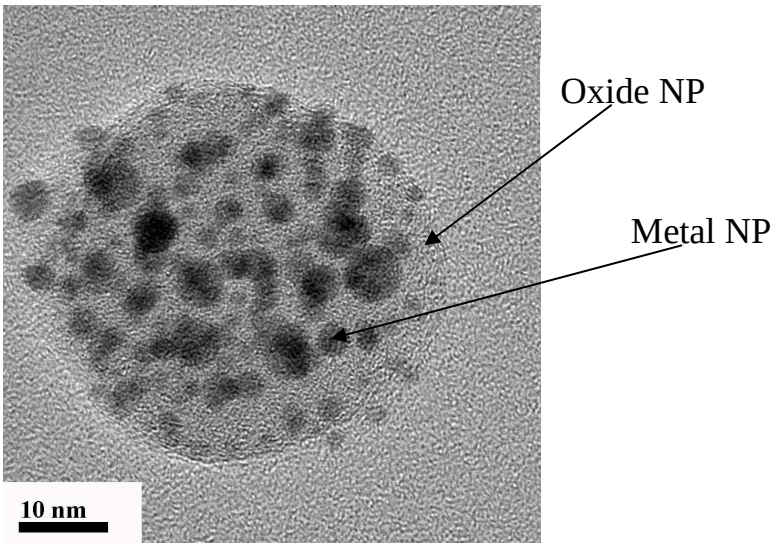

Figure 3.2.4: TEM micrograph of gold on silica NPs.

Chapter 4: Feedstock Particle Synthesis

Titania, silica, gold, and silver micron-sized powders were used as feedstock particles for our process. Silver and gold microparticles were obtained from Dupont Inc. The oxide particles were prepared in our laboratory via a hydrolysis-precipitation mechanism. The synthesis processes for the oxide particles were so chosen to produce spherical particles, with sizes greater than 1 μm.

Section 4.1: Titanium Dioxide Microparticles

The synthesis method reported by L.Wang *et al.* [47] was used to prepare mesoporous titania microsphreres for our study. The synthesis principle is based on the natural outgrowth of inorganic–organic hybrids in static 1-propanol solvent via the slow hydrolysis of $Ti(OPr)_4$ promoted by atmospheric humidity. Neutral surfactant dodecylamine was employed as a template to combine with titanium tetraisopropoxide ($Ti(OPr)_4$) precursor.

In a typical preparation, 0.7 g of $Ti(OPr)_4$ (2.46 mmol) and 0.5 g of dodecylamine (2.70 mmol) are mixed with 20 mL of 1-propanol and further stirred for 15 min, and then the solution is left in an open container without stirring at room temperature for 48 h. The resulting precipitates are separated by decantation from the solution and dried at room temperature overnight to produce as-made sample. The microparticles as prepared have a spherical morphology and a narrow

size distribution (mean diameter ~ 4.2 μm), as shown in Figure 4.1.1 (a). EDS analysis (Figure 4.1.1 (b)) of the as made samples showed no impurities. The particle sizes of 127 particles were calculated using the automated particle analysis technique described in Chapter 3 using Image J1.41o and the particle size distribution is shown in Figure 4.11 (c).

(a)

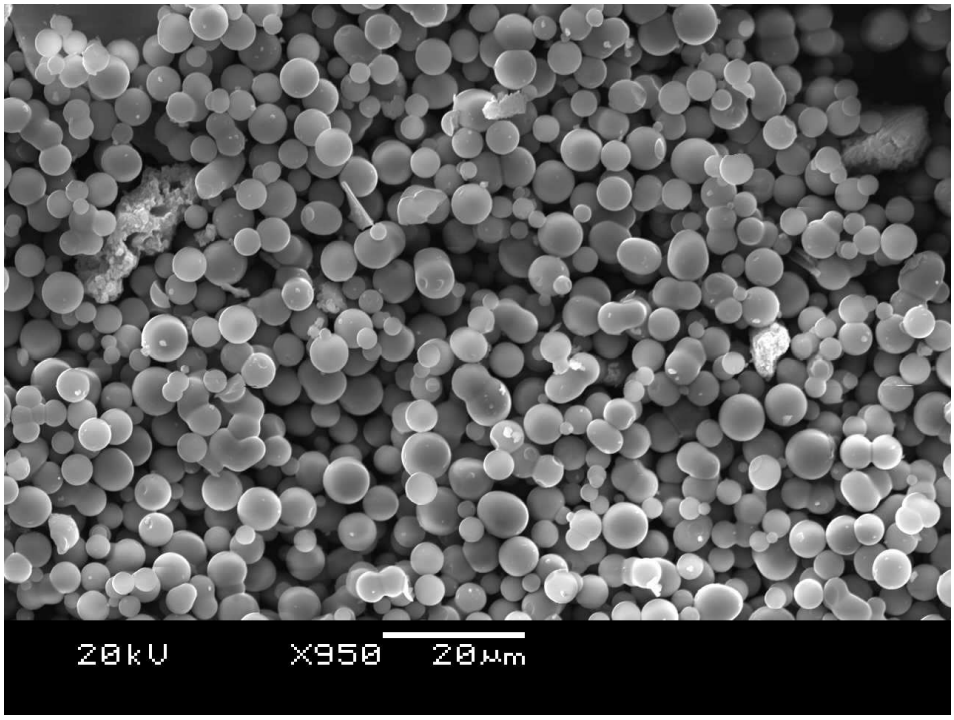

(b)

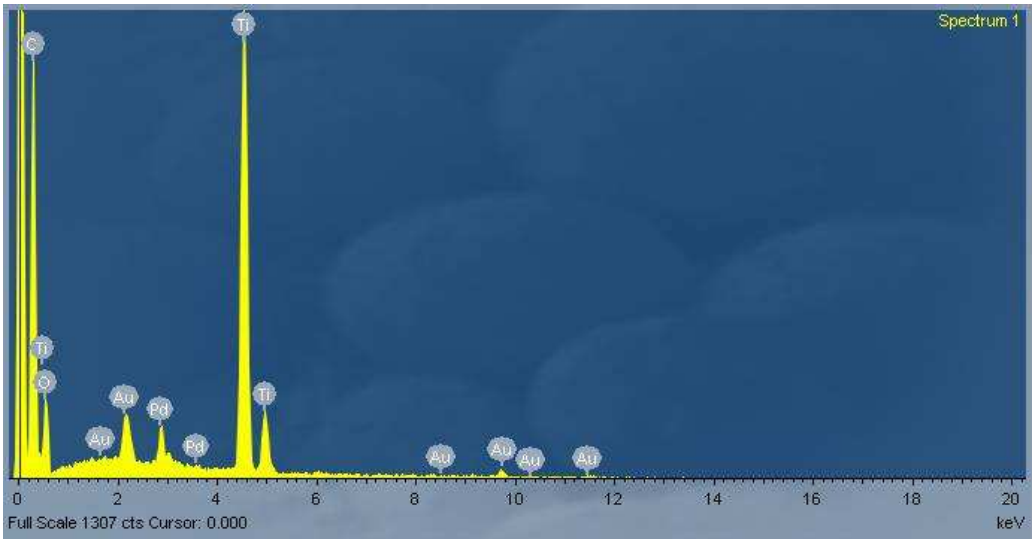

(c)

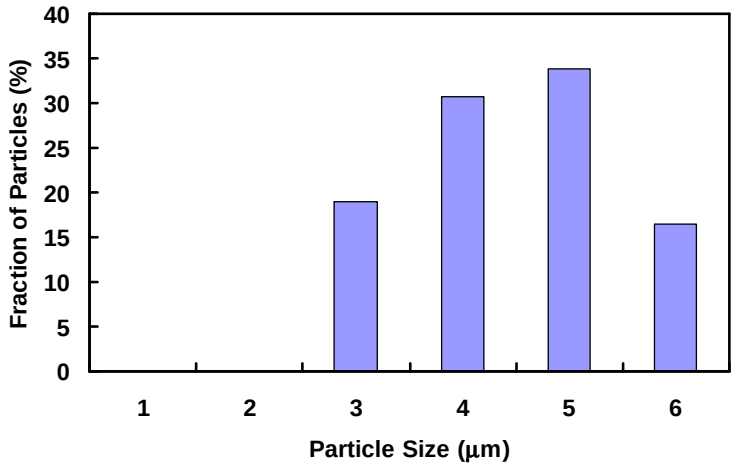

Figure 4.1.1 (a) SEM micrograph of as prepared feedstock TiO_2 microparticles (b) EDS spectrum of feedstock TiO_2 microparticles showing no impurities (c) Particle size distribution of feedstock TiO_2 particles (calculated from 127 particles).

Section 4.2 Silica Particles

Silica microspheres were prepared by following the synthesis method reported by De *et al.* [48]. Silica microspheres were prepared by hydrolyzing Tetraethyl Orthosilicate (TEOS) with doubly distilled water in the presence of acetic acid. TEOS was added to a mixture of acid and water while stirring (rate ~ 550 rpm) at room temperature. TEOS, water and acetic acid were mixed in a molar ratio of 1:4:4. The mixture was stirred in an open container for 15 min and was then quickly filtered and washed successively with ethanol and acetone. The washed solution was then left to dry overnight to obtain uniformly sized silica microspheres of mean particle size 3 μm. The SEM images of the silica microspheres are shown in Figure 4.2.1 (a). EDS analysis (Figure 4.2.1 (b)) of the as-made samples showed no impurities. The particle sizes of 173 particles were calculated using Image J 1.41o and the particle size distribution is shown in Figure 4.2.1 (c).

(a)

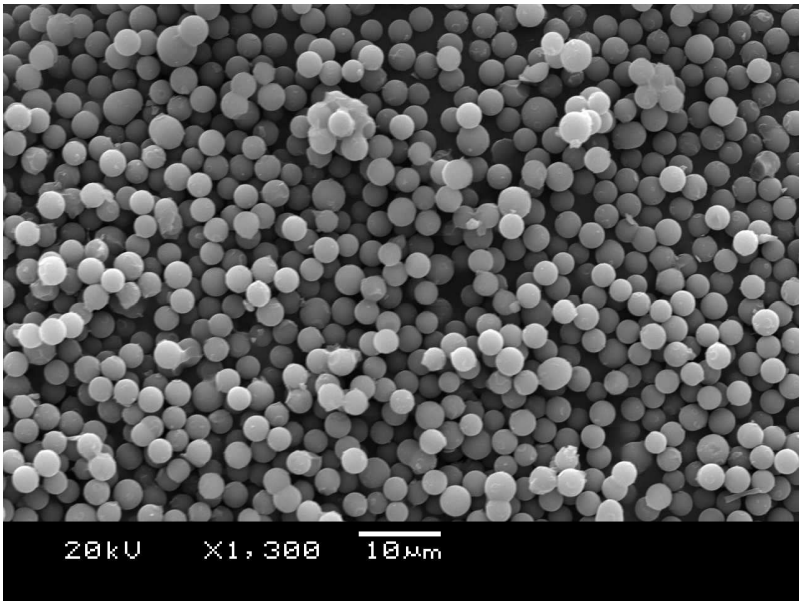
20kU X1,300 10µm

(b)

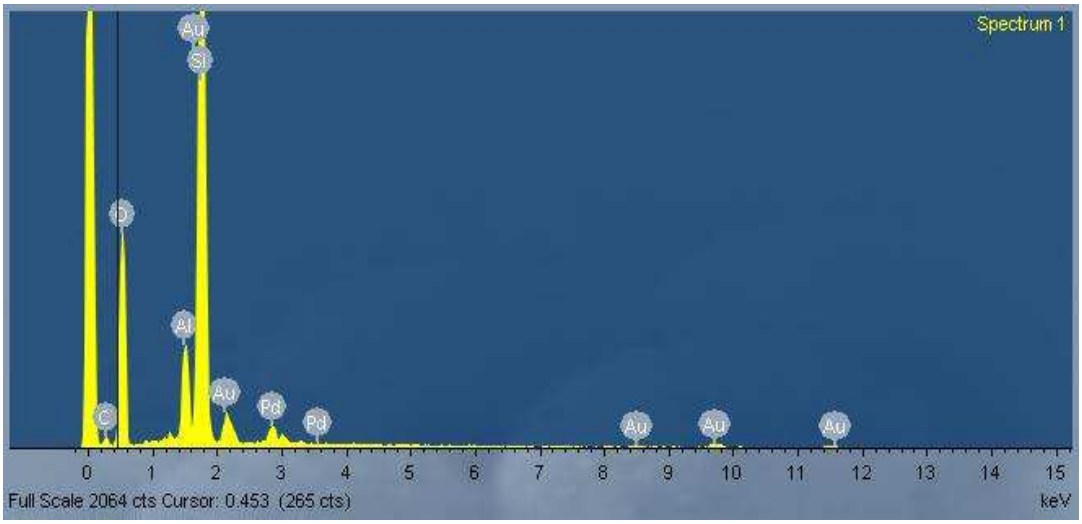
Spectrum 1
Au
Si
O
Al
Au
Pd
Pd
C
Au
Au
Au
0 1 2 3 4 5 6 7 8 9 10 11 12 13 14 15
Full Scale 2064 cts Cursor: 0.453 (265 cts)
keV

(c)

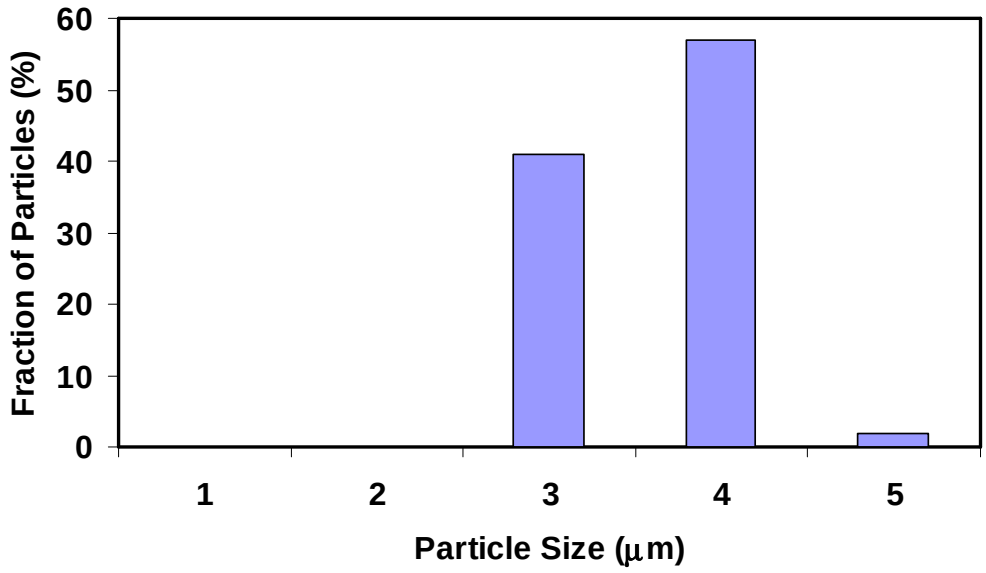

Figure 4.2.1 (a) SEM micrograph of as prepared feedstock SiO_2 microparticles (b) EDS spectrum of feedstock SiO_2 microparticles showing no impurities (c) Particle size distribution of feedstock SiO_2 particles (calculated from 173 particles).

Section 4.3 Gold Microparticles

Gold microparticles (mean particle size ~ 1.3 μm) were obtained from Dupont Inc. The morphology, particle size distribution and EDS analysis of the particles is shown in Figure 4.3.1. A sample set of 88 particles were used to calculate the particle size distribution.

(a)

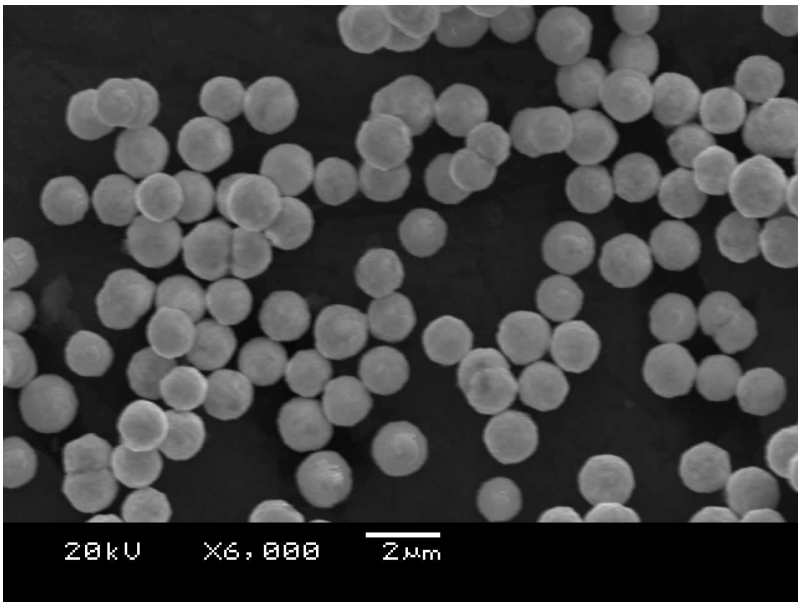
20kU X6,000 2µm

(b)

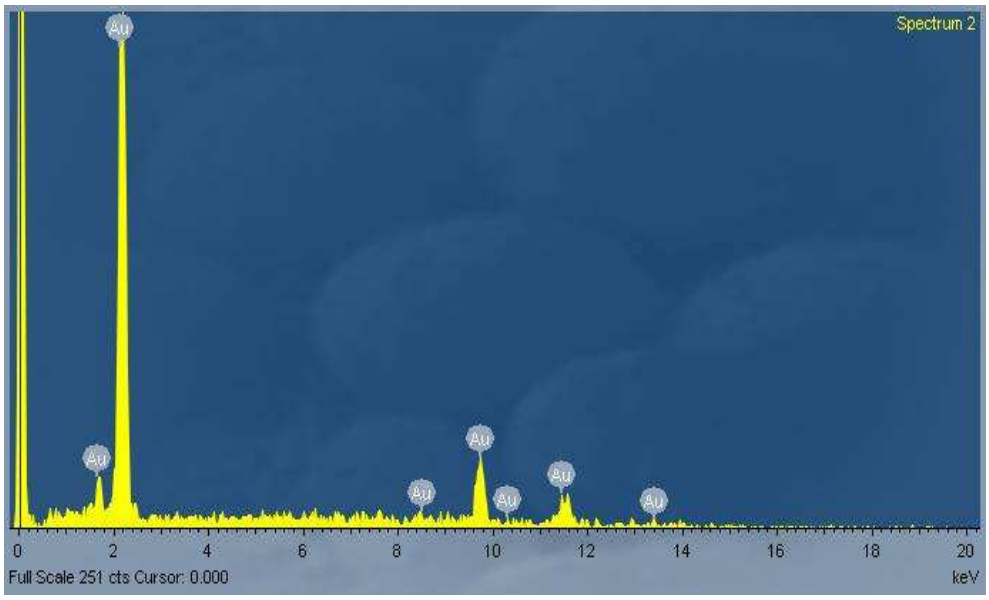
Spectrum 2
Au
0
2
4
6
8
10
12
14
16
18
20
Full Scale 251 cts Cursor: 0.000
keV

(c)

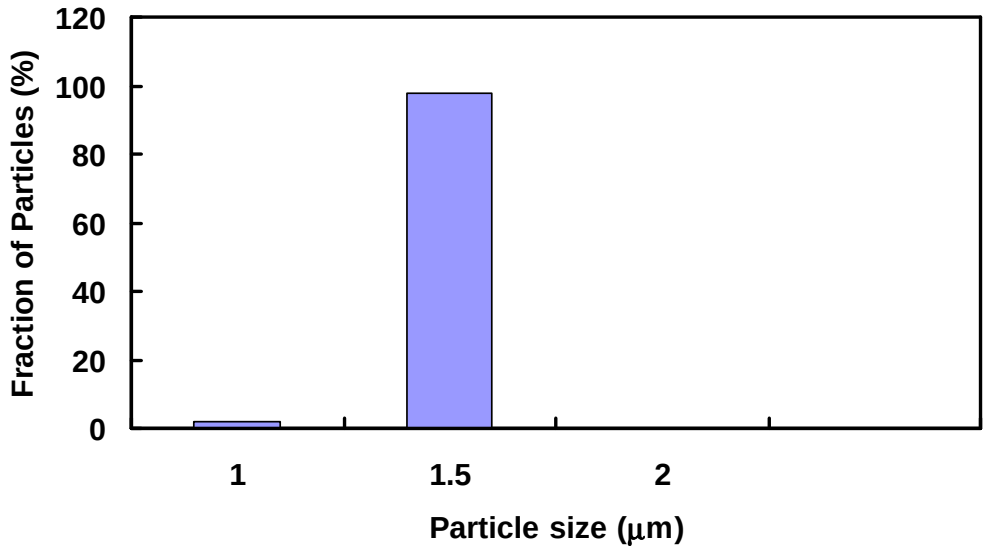

Figure 4.3.1 (a) SEM micrograph of feedstock Au microparticles (b) EDS spectrum of feedstock Au microparticles showing no impurities (c) Particle size distribution of feedstock Au particles (calculated from 88 particles).

Section 4.4 Silver Microparticles

Silver microparticles were obtained from Dupont Inc. The morphology and particle size of the particles is shown in Figure 4.4.1. The silver microparticles are coated with an organic surfactant, which tends to cause agglomeration on the absorption of moisture as shown in Figure 4.4.2.

(a)

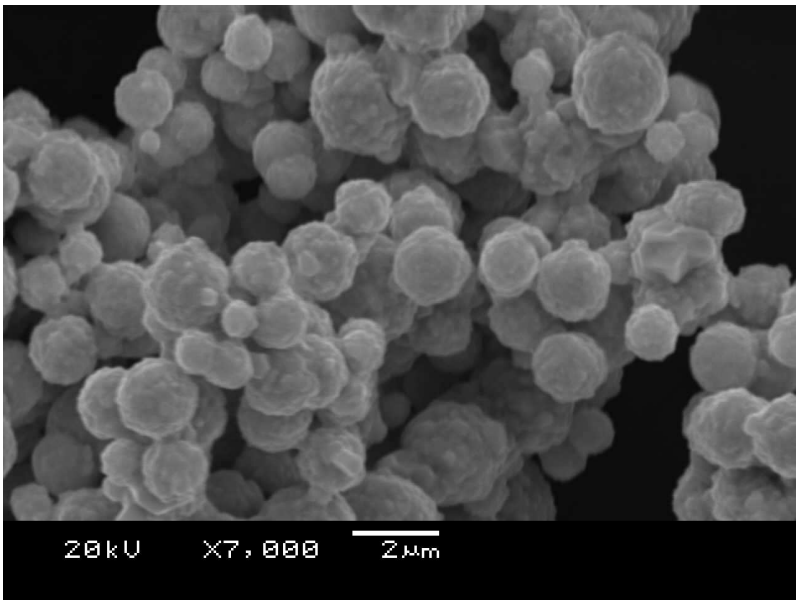
20kV X7,000 2µm

(b)

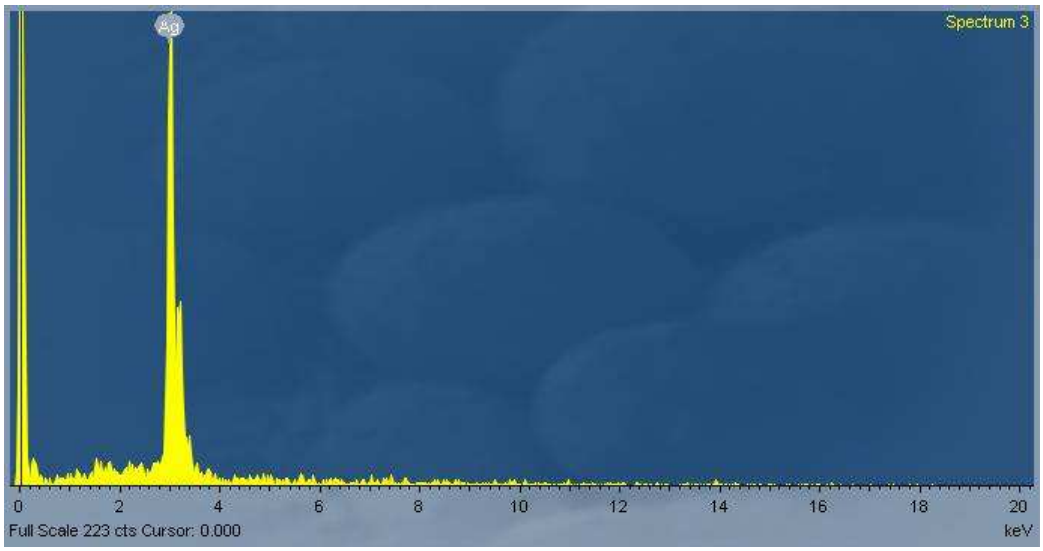
Spectrum 3
Ag
0 2 4 6 8 10 12 14 16 18 20
Full Scale 223 cts Cursor: 0.000
keV

(c)

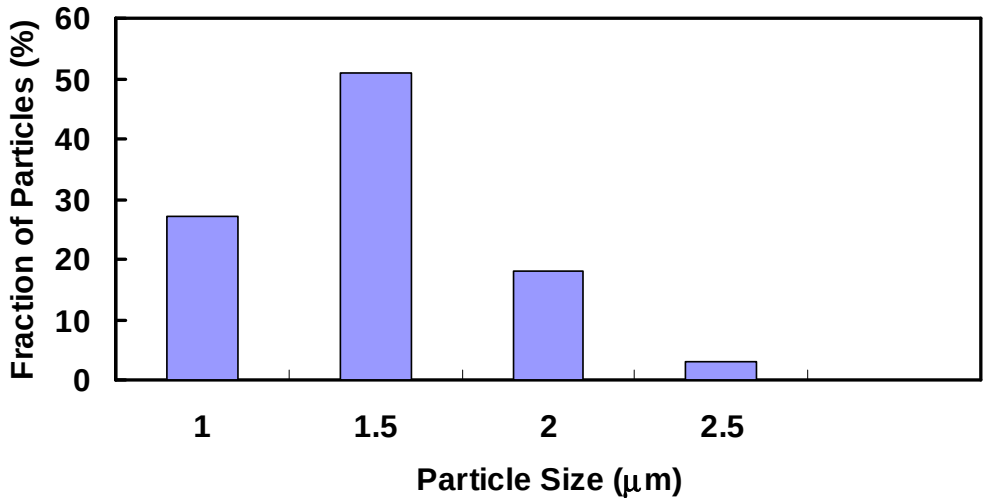

Figure 4.4.1 (a) SEM micrograph of feedstock Ag microparticles (b) EDS spectrum of feedstock Ag microparticles showing no impurities (c) Particle size distribution of feedstock Ag particles (calculated from particles).

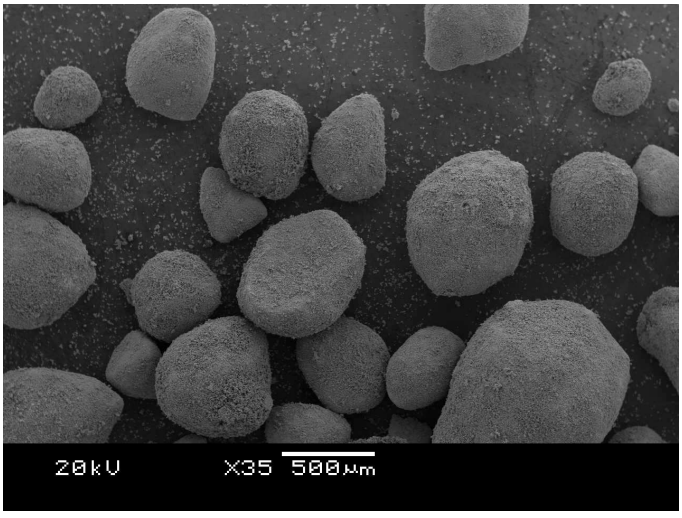

Figure 4.4.2: SEM micrograph of Ag microparticles after long exposure to moisture.

Chapter 5: Results and Discussion

Section 5.1: Metal on Oxide NPs

Our metal-on-oxide NP fabrication technique described in Section 2.4 is, in principle, capable of producing most combinations of metals on oxides. The feasibility of the process depends on 3 factors – 1. The capability to produce feedstock microparticles 2. The flow of the microparticles 3. The ability of the microparticles to absorb laser energy and ablate. Most materials can be synthesized in microparticulate form with existing synthesis techniques. However, the size of the microparticles and shape is also a relevant factor for them to ablate. Dielectrics, for example do not absorb laser energy and generate a shockwave, unless they are spherical in nature. Spherical dielectric microparticles above a certain size (different for each material) can focus the laser beam at the rear end of the particle and initiate plasma breakdown. On the other hand, metal particles, above a certain size, can absorb laser energy irrespective of their shape. However, particles with poor flowability makes it difficult to aerosolize them (e.g. dielectrics such as silica or irregularly shaped powders which tend to agglomerate easily), and therefore adjust the relative amount of core and shell materials. Metal and dielectrics with similar flowability are therefore ideal for the LAM process.

To demonstrate the capability of this process to produce a range of metal-oxide NPs, Au-TiO_2, Ag-TiO_2 and Au-SiO_2 NPs were produced and are shown in

Figures 5.1.1 – 5.1.3. All NPs mentioned in the current section were produced at a laser fluence of 1 J/cm^2 and using He as the buffer gas. The NPs consist of smaller 1 – 5 nm metal NPs dispersed on the surface of the larger 10 – 40 nm oxide NPs.

Gold on Titania NPs

Smaller 1 – 5 nm gold NPs dispersed on larger 10 – 60 nm oxide particles were prepared. The flowability of gold particles was much higher than that of titania, and thus the frequency of the solenoid used to aerosolize titania powder was kept higher than for that used to aerosolize the gold.

The NPs were characterized using a JEOL 2010F TEM, Figure 5.1.1. TEM micrographs show an absence of lattice fringes for titania NPs, suggesting that they are amorphous. The non-uniformity in the size of the titania NPs is due to the higher breakdown threshold for NP formation of titania microparticles, which results in a significant number of titania NPs being formed via evaporative heating mechanism instead of shockwave mechanism. Gold NPs, have a much lower breakdown threshold and have a narrower size distribution. Also, titania NPs tend to agglomerate during the process, while gold NPs are well dispersed on the titania surface.

(a)

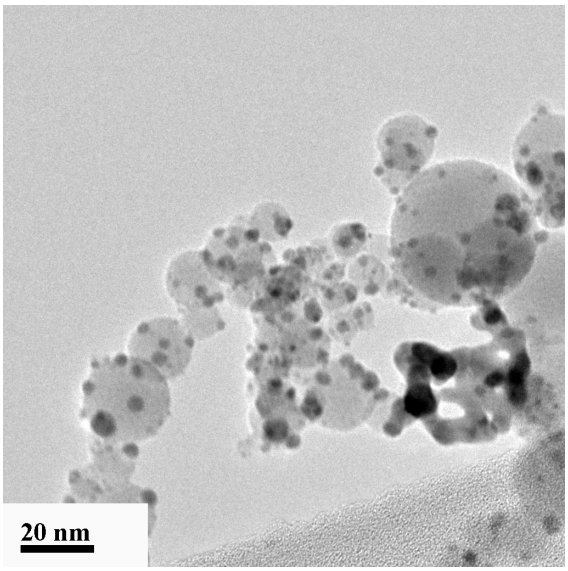

(b)

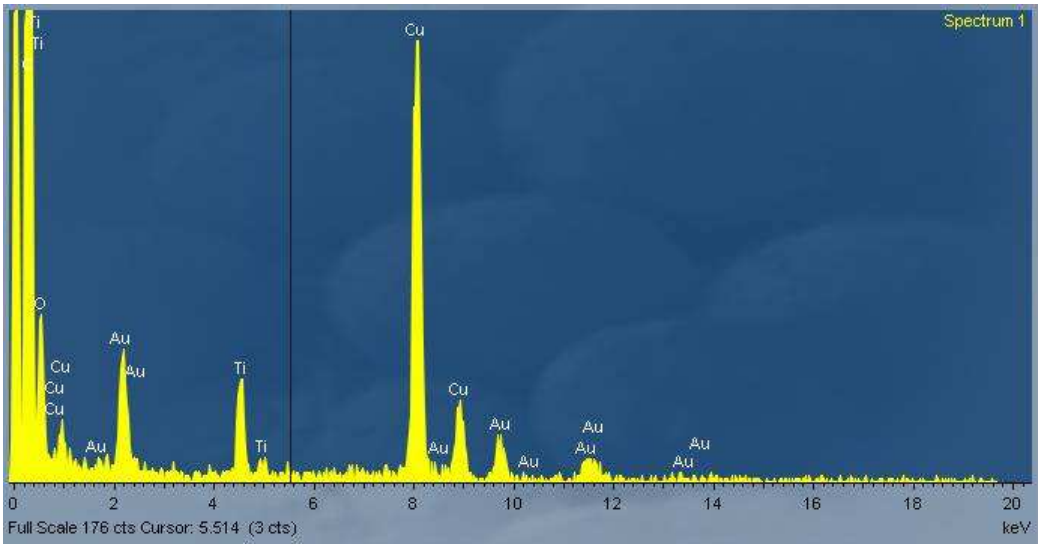

Figure 5.1.1: (a) TEM micrograph of Au on TiO_2 NP (b) EDS analysis of the NPs.

Silver on Titania NPs

Smaller 1 – 5 nm silver NPs dispersed on larger 10 – 60 nm oxide particles were prepared. The flowability of silver particles was even higher than that of gold, and thus the frequency of the solenoid used to aerosolize silver was kept at a minimum (1 Hz). These particles were prepared using He as the carrier gas and at a laser fluence of 1 J/cm^2. The TEM micrograph and EDS analysis of the NPs are shown in Figure 5.1.2. Similar to gold on titania NPs, titania particles tend be exhibit a broad size distribution and agglomerate into long chains of NPs.

(a)

.

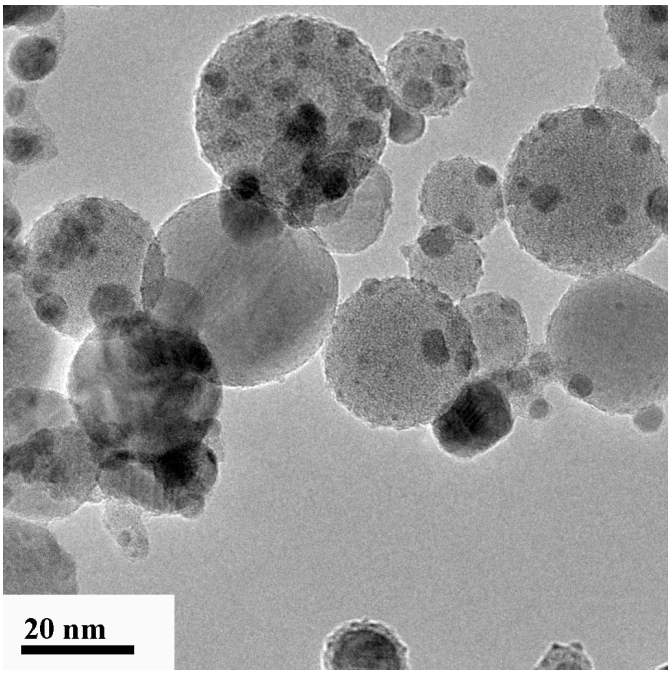

(b)

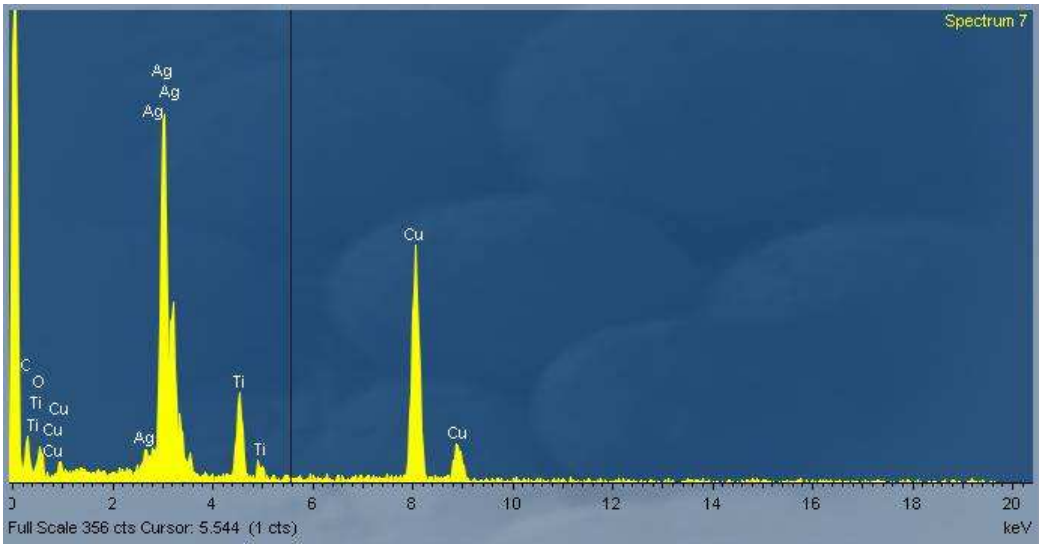

Figure 5.1.2: Figure 4.1.1: (a) TEM micrograph of Ag on TiO_2 NP (b) EDS analysis of the NPs.

Gold on Silica

Smaller 1 – 5 nm gold NPs dispersed on larger 10 – 60 nm oxide particles were prepared. The flowability of silica was extremely poor, thus it was required to increase the frequency of the solenoid to a maximum for silica particles and reduce it to a minimum for gold microparticles. A TEM micrograph of the NPs is shown in Figure 5.1.3. Elemental composition line mapping using EDS was done on these samples to show the relative positions of gold NPs and silica NPs as shown in Figure 5.1.4. Silica particles obtained by our process were of varied shapes and very agglomerated, as shown in Figure 5.1.5.

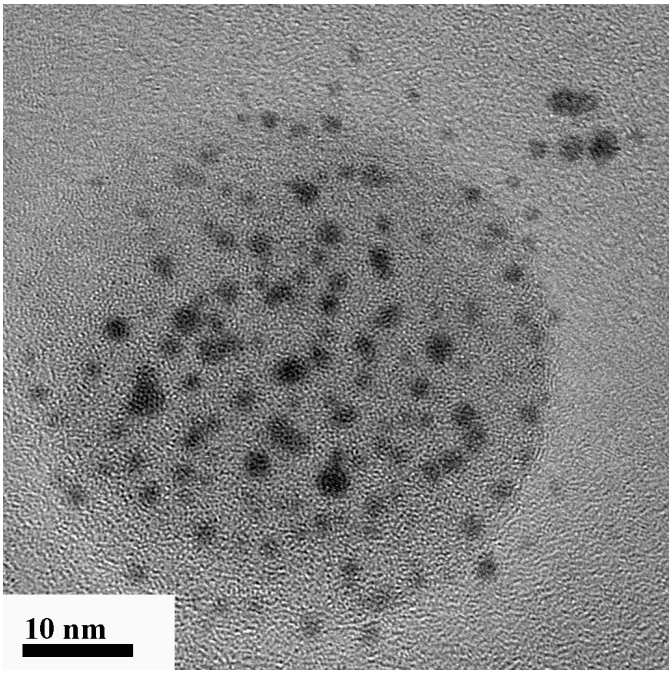

Figure 5.1.3: TEM micrograph of gold on silica NP.

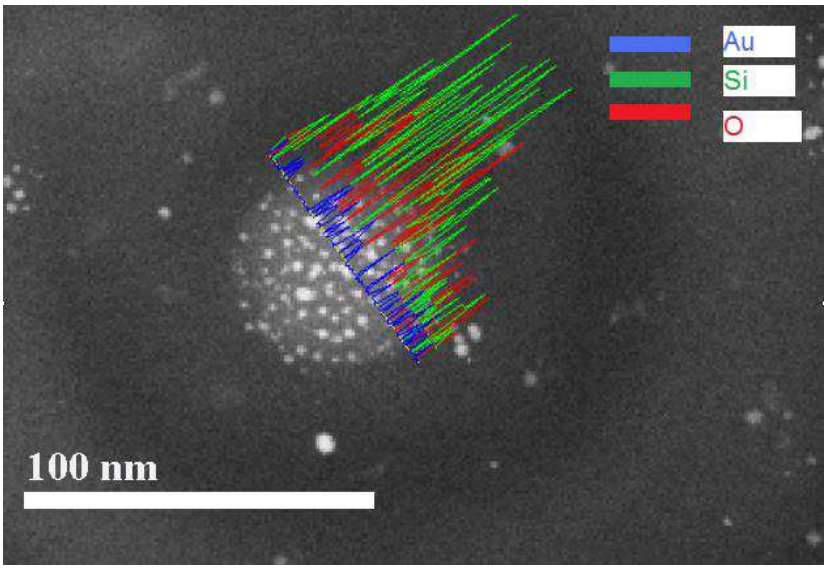

Figure 5.1.4: Line mapping of a Au-SIO_2 NP.

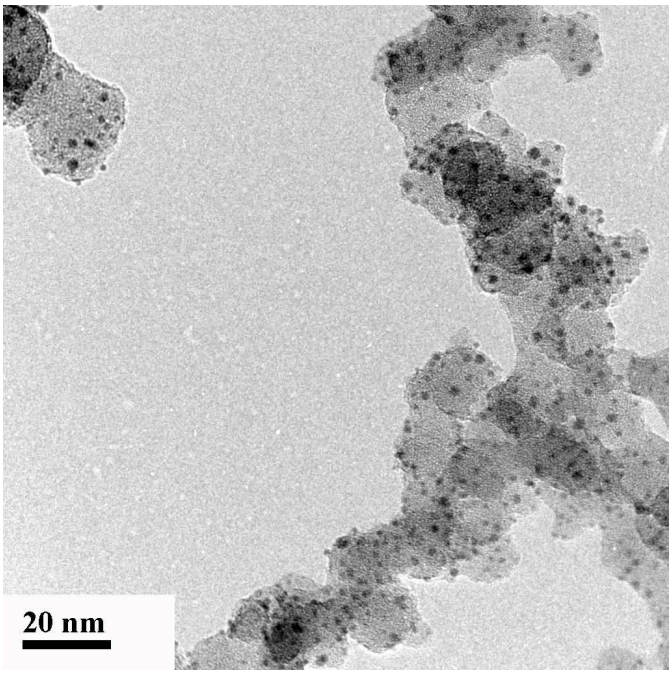

Figure 5.1.5: Gold on silica NPs produced by the double ablation LAM process.

Silver on Silica

The differences in flowability of silica and silver microparticles is very large, and hence it was not possible to fabricate silver-on-silica NPs. An improved aerosol generator is needed to solve this problem.

Section 5.2: Effect of Carrier Gas

Figure 5.2.1 shows TEM images of TiO_2-Au NPs produced using He, Ar, and a mixture of He-Ar carrier gasses. It is apparent from the micrographs that the mean particle size of both the oxide core and metal NPs increased when using a

heavier molecular weight carrier gas. Analyses of the particle size distributions, shown in Figure 5.2.2, reveal that the mean sizes of the oxide NPs increased from about 16 nm to 60 nm and the gold NPs increased from about 1.7 nm to about 10.8 nm upon changing the carrier gas from He to Ar. A mixture of Ar and He (in the ratio 50:50) gasses resulted in NP sizes for both the TiO_2 (~ 33 nm) and Au (~ 5 nm) that were intermediate between that for pure He and pure Ar.

These results are consistent with previous results with single component, Ag NPs in which it was found that heavier carrier gasses constrain the expansion of the ablation plume more than lighter gasses [49]. As a result of the denser plume, the collision frequency between the NPs and the ad-atoms from the vapor is increased which results in a greater degree of coalescence, and hence, larger NPs.

The composition of the carrier gas can thus be effectively used to tune the particle size of NPs. A H_2/He mixture (with H_2 under the combustibility limit) could presumably be used to further decrease the particle size.

(a)

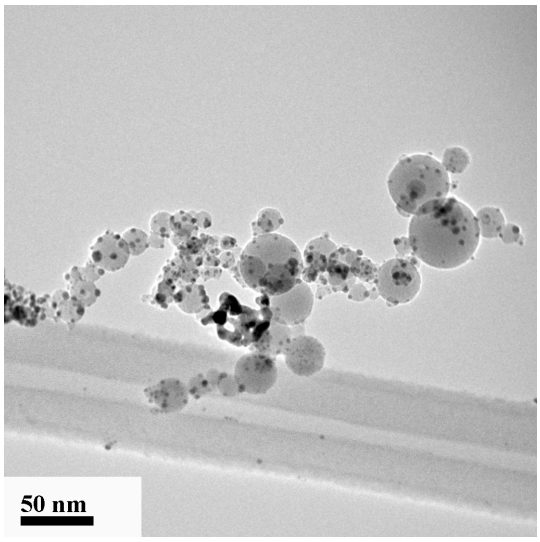

(b)

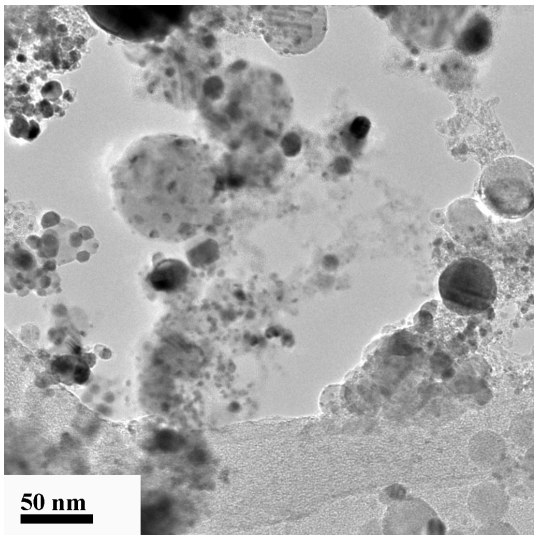

(c)

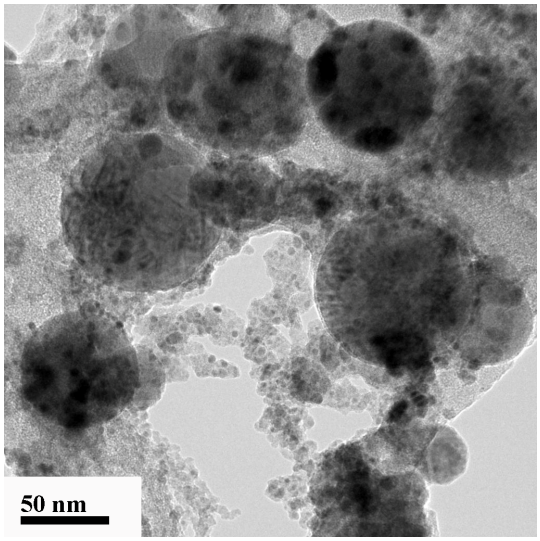

Figure 5.2.1: TEM micrographs of Au-TiO_2 NPs produced at a laser fluence of 1.5 J/cm^2 in (a) He carrier gas (b) 1:1 gas mixture of He and Ar (c) Ar carrier gas.

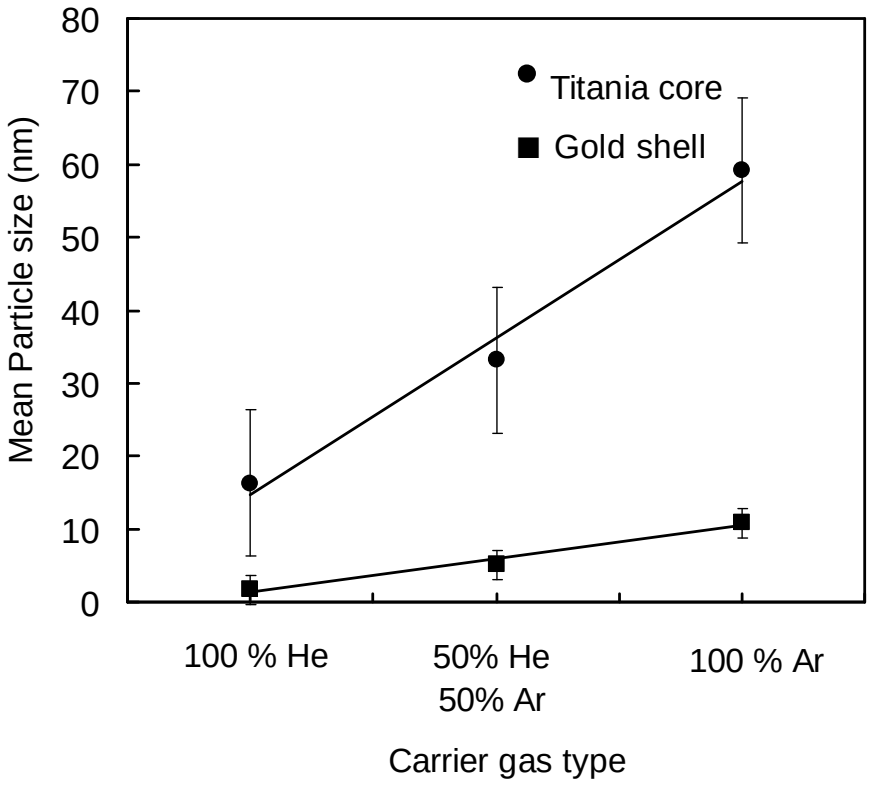

Figure 5.2.2: Influence of carrier gas on the mean particle size for titania core and gold NPs.

Section 5.3: Effect of Laser Fluence

The laser fluence also has been shown to influence the size distributions of the single component NPs. At fluences below the breakdown threshold, the surfaces of the micron-sized feedstock particles are heated, which results in evaporation and then condensation of larger NPs from this vapor. As the laser fluence is increased above the breakdown threshold, the shockwave mechanism for the formation of NPs is more prominent. The compression and

heating that occurs from the shock results in much smaller NPs when compared to the NPs produced from the surface heating mechanism. Since the laser energy pulse is pseudo-Gaussian, at fluences only slightly above the breakdown threshold, a significant fraction of the NPs are produced from surface heating before the fluence reaches the breakdown threshold and initiates the shock-driven process. As the fluence is increased further, the relative fraction of NPs produced from the surface heating process decreases whereas the fraction of smaller NPs from the shock driven process increases.

The influence of laser fluence on gold NP size distribution is shown in Figure 5.3.1. A higher laser fluence of 1.5 J/cm^2 gave a narrower particle size distribution with a smaller mean particle size when compared to a fluence of 1 J/cm^2. All subsequent experiments were thus carried out at 1.5 J/cm^2 to ensure that the majority of the NPs were produced by the shock-driven mechanism rather than from the surface heating mechanism.

(a)

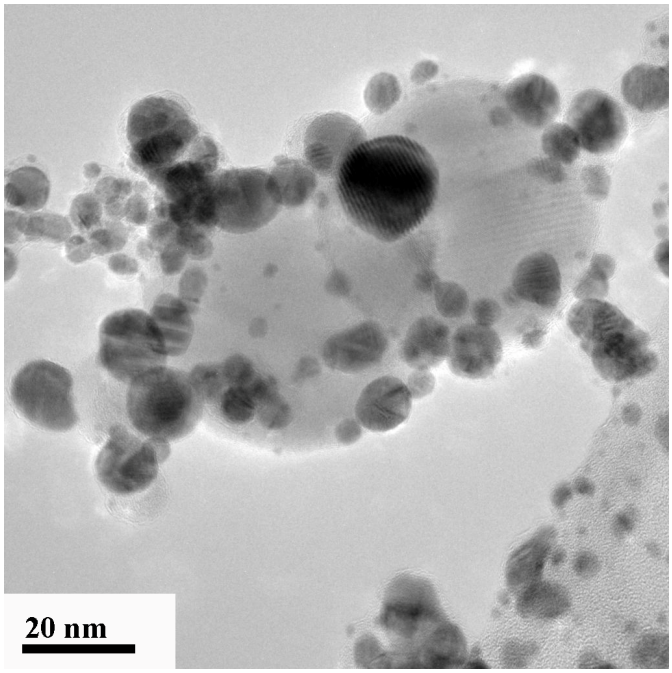

(b)

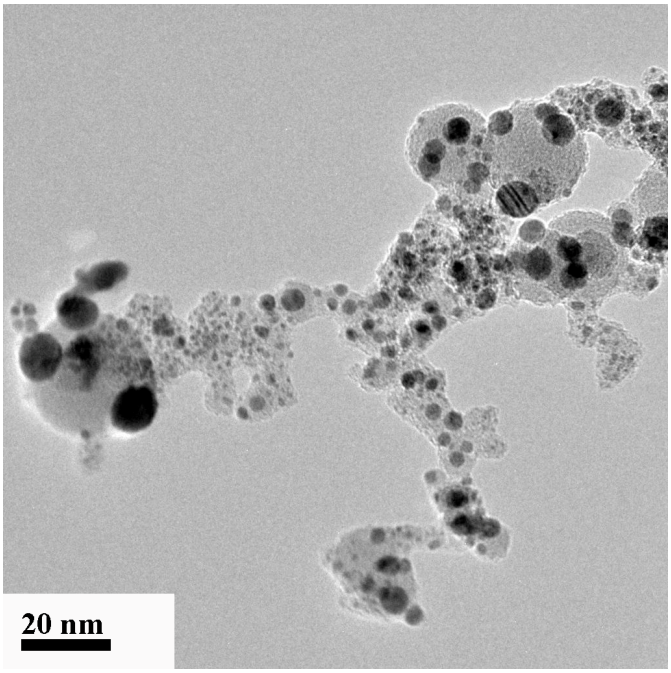

(c)

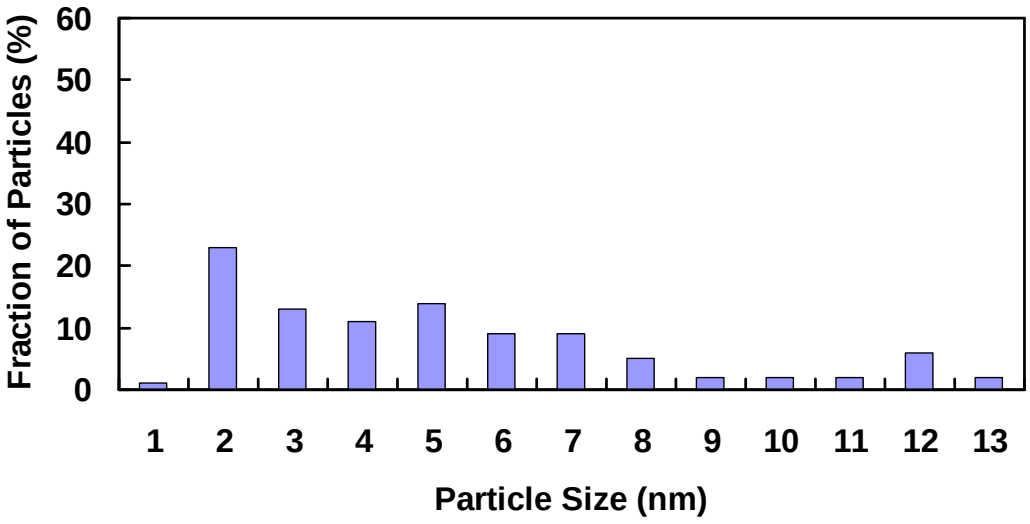

(d)

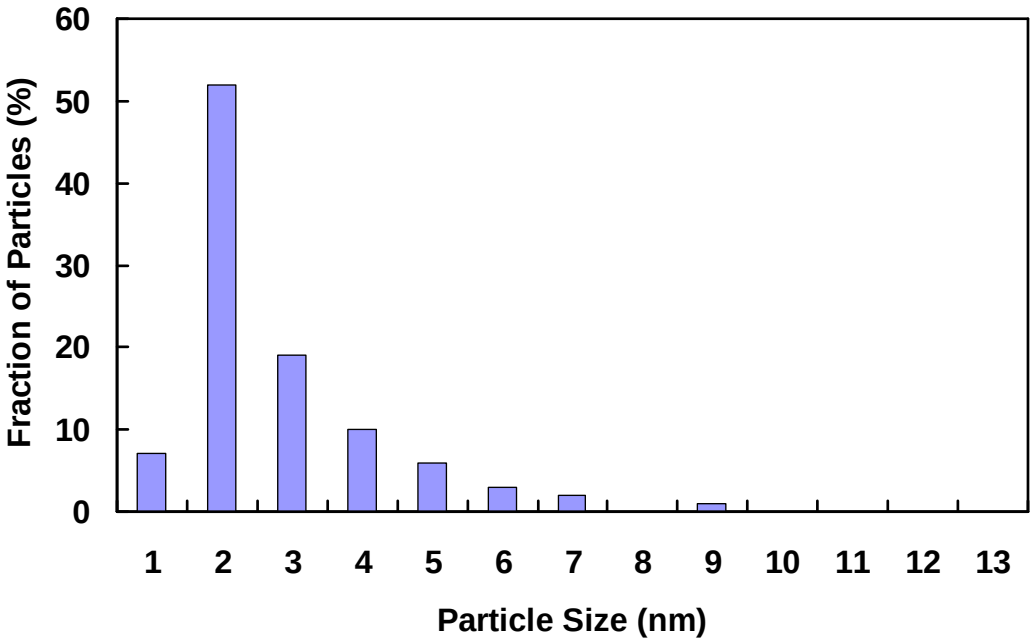

Figure 5.3.1 TEM micrographs of Au-TiO_2 NPs produced in He carrier gas at a laser fluence of (a) 1 J/cm^2 (b) 1.5 J/cm^2. Particle size distribution of Au NPs produced at a laser fluence of (c) 1 J/cm^2 (calculated from 100 particles) and (d) 1.5 J/cm^2 (calculated from 272 particles).

Section 5.4: Non-Agglomerated NPs

It is evident from the TEM images that the oxide NPs particles tended to agglomerate during the process, whereas the metal NPs were well-dispersed on the oxide surfaces. Previously, it has been shown that NPs are ionized during the ablation process and thus electrostatically repel each other [49]. However, agglomeration is possible when recombination of the ionized oxide NPs with the free electrons occurs in the aerosol. This causes the NPs to lose their charge, and agglomeration then occurs due to attractive Van-der-Waals forces. In these experiments with multi-component NPs, the oxide NPs travel a much longer distance before they are captured onto the TEM grids compared to the metal particles that are captured on the oxide surface during condensation. The long travel distances likely makes the oxide NPs more susceptible to recombination and hence agglomeration.

This hypothesis was tested by collecting only TiO_2 particles with a shortened collection distances (~ 6 cm) compared to the earlier experiments (~ 16 cm). The results, shown in Figure 5.4.1 show individual oxide NPs with no evidence of agglomeration. This confirms that when the collection times are short, it is possible to collect unagglomerated NPs.

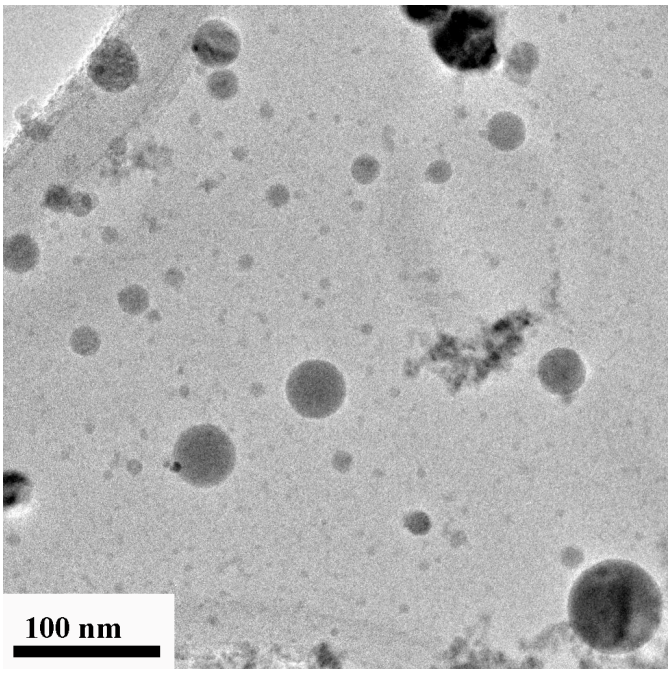

Figure 5.4.1: TEM micrograph of titania NPs deposited with shortened collection distance showing reduced agglomeration.

The approach discussed in Section 4.4 utilizes the alternative method for producing and collecting NPs. As can be seen in Figure 5.4.2, it was possible to make metal-on-oxide particles with minimal agglomeration using this method. Since this approach relies on turbulent flow, it is possible to have unequal flows for oxide and metal particles and thus vary the amount of both by the individual flows, giving an abundance of titania NPs and avoiding free gold NPs. However, this approach suffers from major drawbacks – 1. There is limited control over titania particle size, since the microparticle aerosol path is coincident with the laser beam and they thus undergo ablations multiple times 2. titania NPs are deposited

all over the chamber 3. the process may produce gold NPs that stick onto the surface of the titania NPs, instead of nucleating on the titania NPs 4. NPs are deposited on the front window, damaging the MgF coating.

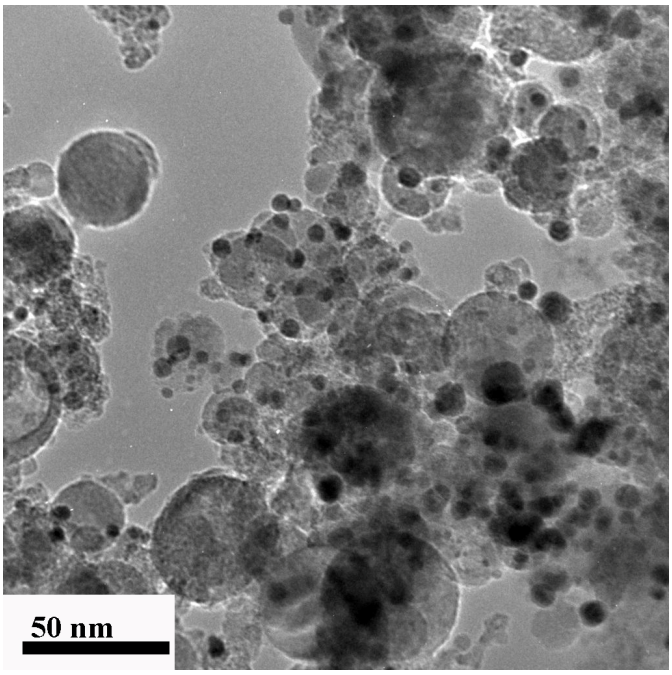

Figure 5.4.2: TEM micrograph of Au-TiO_2 NPs deposited with using the alternate method (showing reduced agglomeration).

Section 5.5 Effect of Electron Bombardment on Stability of NPs

The dependence of gold NPs' catalytic activity on their size requires them to not sinter at operating temperatures [38]. It has been previously shown that Au NPs tend to sinter at higher temperatures [41], thus losing their catalytic properties. Preliminary heating experiments using the electron beam of a TEM were thus performed to study the stability of Au NPs produced by our method. These

experiments rely on focusing of the electron beam of a known electron dose, on the NPs, and observing the resulting nanoscopic changes [50]. Electron dose [51] in a TEM is defined as the charge density (which is the total number of electrons / per unit area) hitting the specimen. Inelastic collision of electrons with the specimen can heat up the specimen. However, specimen heating is difficult to measure experimentally because of the many variables that can affect the result, such as thermal conductivity, emissivity, thickness and the surface conditions of the specimen and the beam size, energy and current. An attempt to predict the effect of beam current and thermal conductivity on sample temperature was done by Hobbs [52]. The results show that for good conductors such as a metal, heating is negligible, while for insulators such as TiO_2 heating could be quite substantial. Electron bombardment can also lead to the sputtering of surface atoms of the particles, surface diffusion of atoms and the formation of point defects in the particles. A variety of complex phenomenon occur due to the interaction of electrons with NPs, which though not completely understood, give us some qualitative insight into the stability of the NPs.

Sintering of free Gold NPs

Free gold NPs (NPs not sitting on titania particles) of two different mean sizes (5-6 nm and 2-3 nm) were exposed to an electron dose of 460-480 pA/cm^2. Figures 5.5.1 and 5.5.2 show the sintering stages of the larger particles and smaller

particles, respectively. As expected, the larger gold NPs sinter at a slower rate. Neck formation and some sintering is apparent for the larger particles, while the smaller particles completely sinter into a single particle within a span of 40 seconds.

(a)

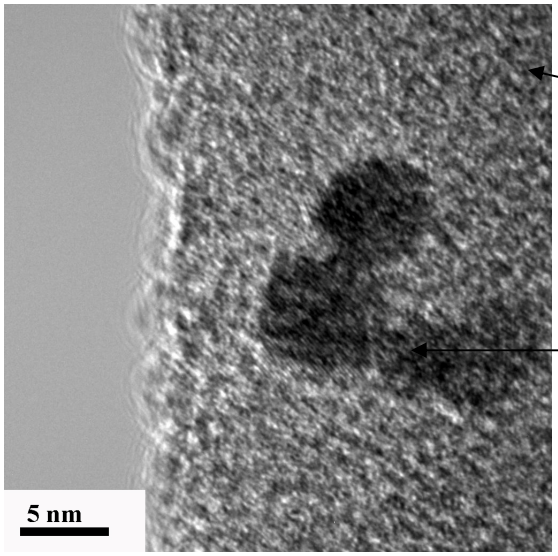

(b)

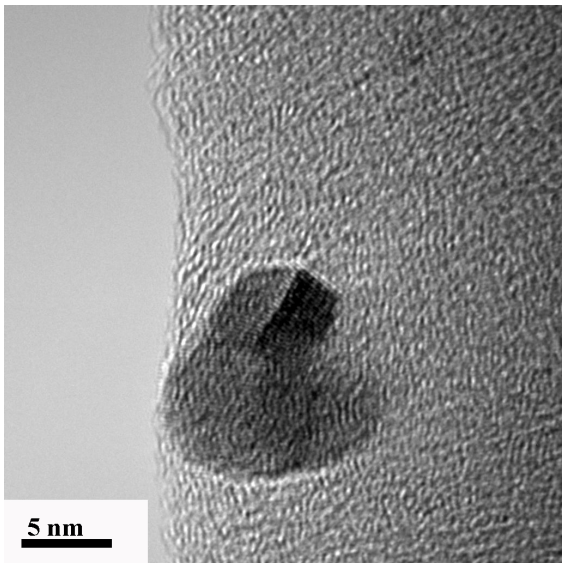

(c)

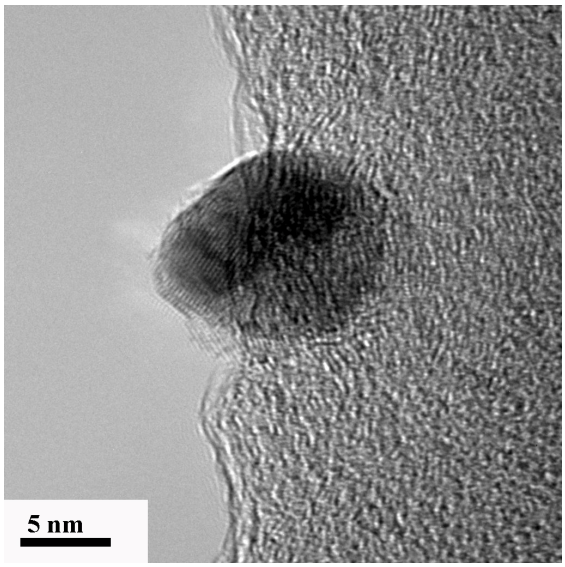

Figure 5.5.1: TEM image of larger Au NPs exposed to an electron dose of 460-480 pA/cm^2, after (a) 0 sec (b) 90 sec (c) 180 sec.

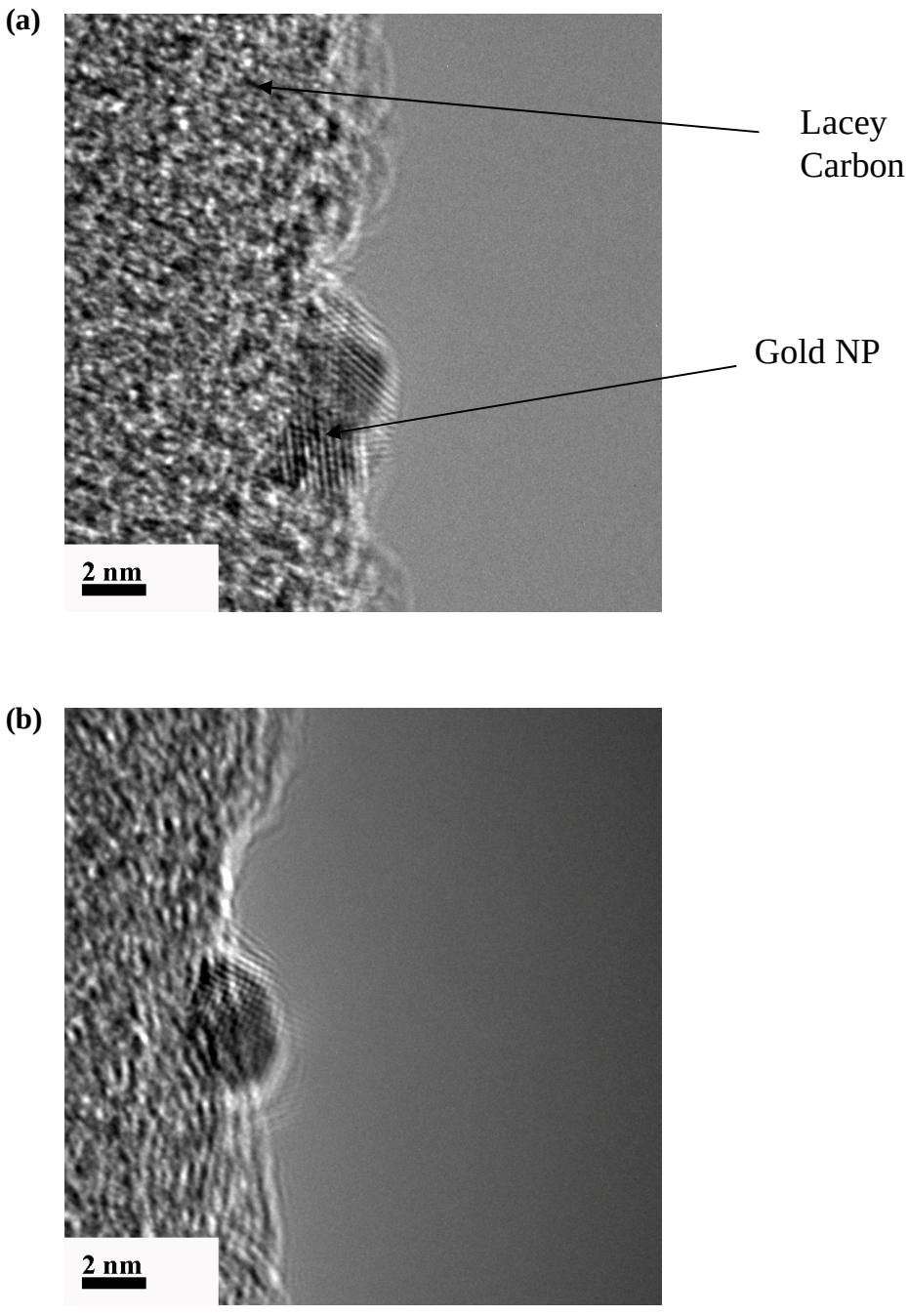

Figure 5.5.2: TEM image of smaller Au NPs exposed to an electron dose of 460-480 pA/cm^2, after (a) 0 sec (b) 40 sec.

Sintering of Gold NPs on Titania Surfaces

Gold NPs on titania NPs showed a peculiar sintering behavior. Two such particles were observed and are characterized in Figure 5.5.3. One of the studied systems consisted of three small Au NPs (size ~ 4 nm) on titania NPs, exposed to an electron dose of 470 pA/cm^2. As shown in Figure 5.5.3, the three NPs sintered within a span of 90 seconds into a single lumpy gold NP.

(a)

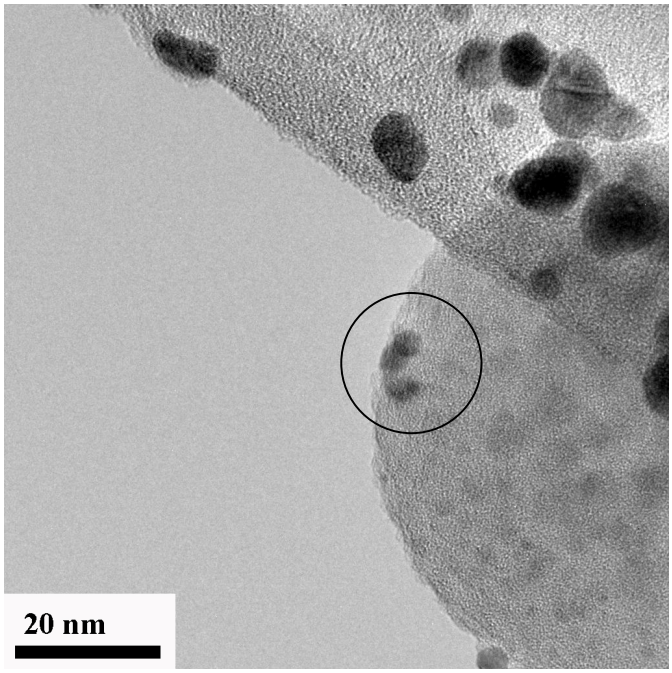

(b)

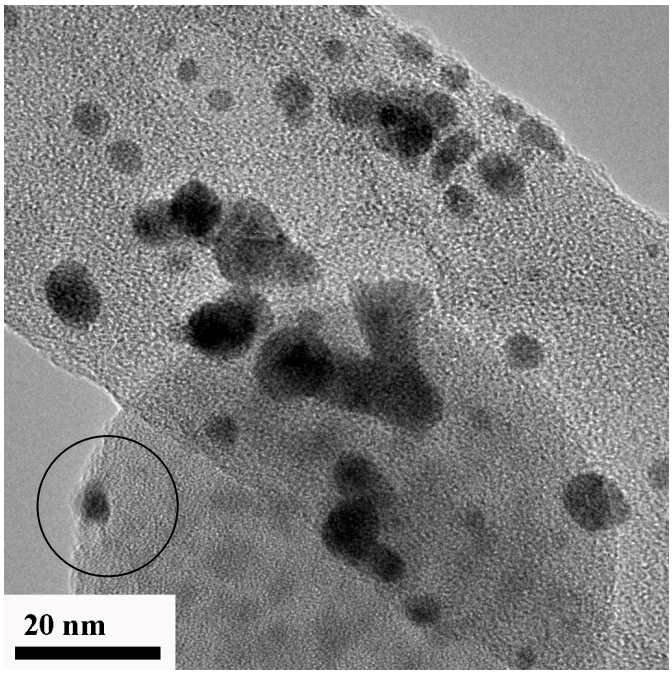

Figure 5.5.3: TEM image of Au NPs on TiO_2 NPs exposed to an electron dose of 470 pA/cm^2, after (a) 0 sec (b) 90 sec.

The other system studied consisted of gold NPs of various particle sizes on a much larger titania particle, exposed to an electron dose of 460 pA/cm^2. The TEM micrographs shown in Figure 5.5.4 show the time-dependent behavior of the gold NPs on the titania substrate at the given electron dose. The effect of electron bombardment caused a very unusual behavior. NP A can be seen to migrate away from the smaller NP C and move towards NP B, eventually forming a neck. NP D seems to migrate freely on the surface of titania. NP C, E, F , G have completely rearranged themselves, without sintering. Certain NPs such as B-D, F-G show a desintering type of behavior. These observations, though not conclusive, give the

following atypical results – (1) A few Au NPs are free to migrate on the surface, while others are possibly pinned to the titania surface (2) In the previous examples smaller NPs of gold, irrespective of whether they were lying freely or on titania substrate, sintered readily. However, many small Au NPs in the present example did not sinter even after long electron beam exposure, while a few larger particles formed necks (3) A few NPs showed an unusual desintering behavior. One possible hypothesis that could explain the differences in behavior of these particles could be the way they attach themselves to the titania surface i.e. whether the Au NPs are simply sticking onto the titania NP or have nucleated on the surface. An alternative hypothesis is based on surface energy anisotropy effects. More controlled experiments using a heating stage could shed light on this peculiar behavior of Au NPs on the TiO_2 surface.

(a)

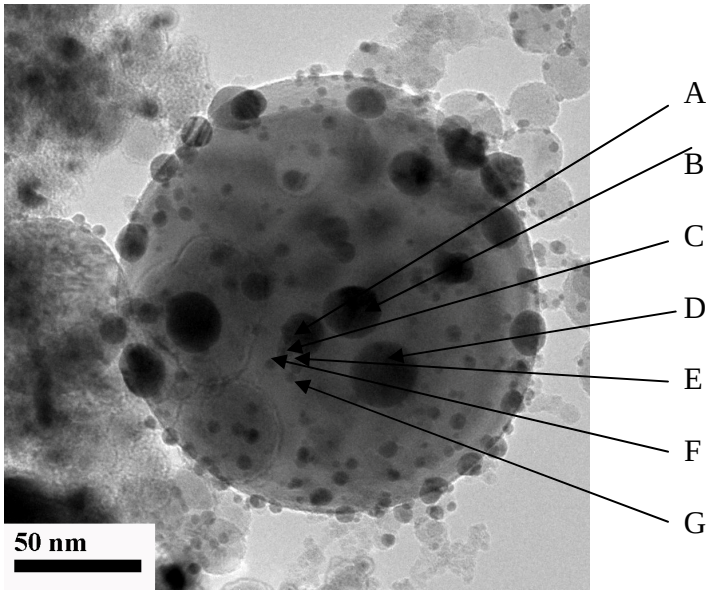

(b)

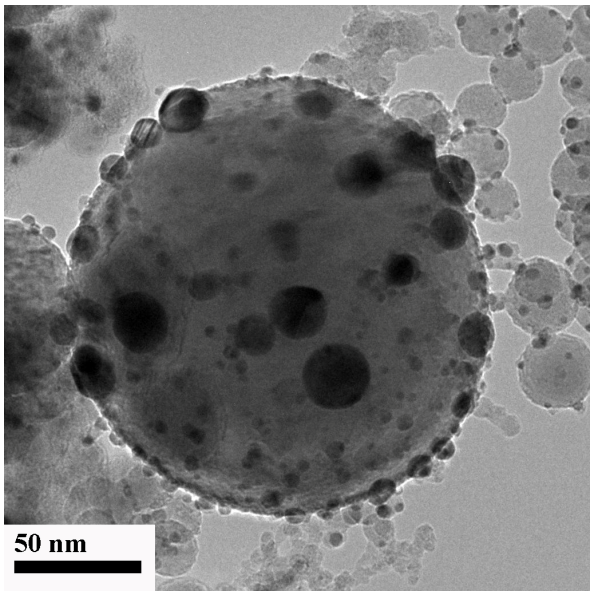

c)

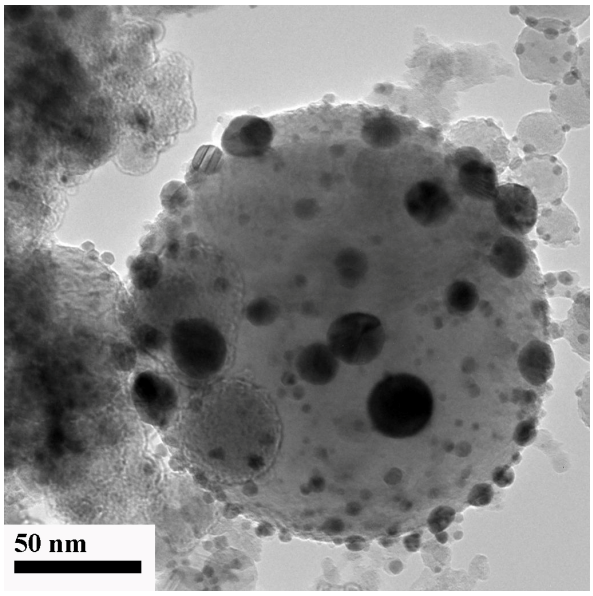

Figure 5.5.4: TEM image of Au NPs on TiO_2 NPs exposed to an electron dose of 470 pA/cm^2, after (a) 0 sec (b) 300 sec (c) 450 sec.

Effect of Electron bombardment on Titania NPs

A TEM micrograph of a titania NP after long exposure to the electron beam in the TEM is shown in Figure 5.5.5. The image shows that the initially amorphous titatnia NP crystallized after long exposure to the electron beam. It is not clear whether TiO_2 crystallization was a result of specimen heating or radiation damage. Similar phenomenon has been previously observed in a number of systems [53,54].

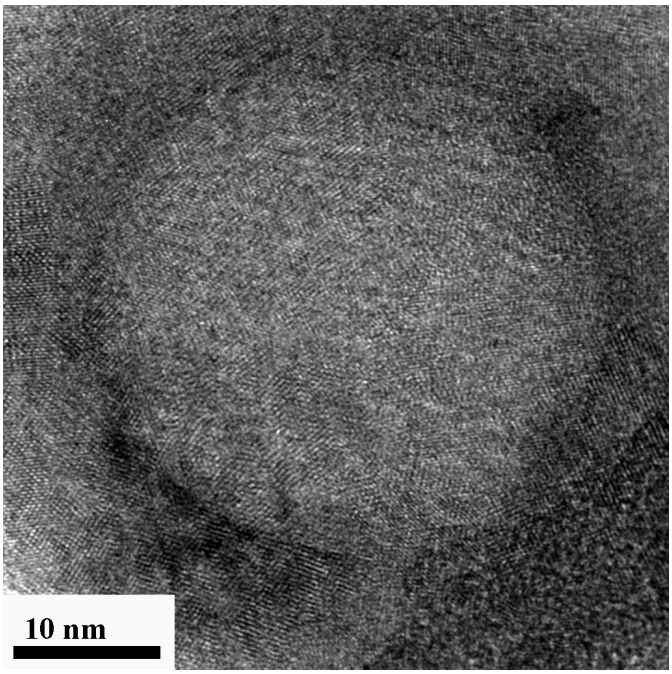

Figure 5.5.5: TEM image of a amorphous TiO_2 – crystalline TiO_2 core shell structure, produced by electron bombardment of an amorphous TiO_2 NP.

Chapter 6: Advantages of the Double Ablation LAM Process

Wet chemical methods have been the primary techniques used to produce multi component, oxide-metal NPs. However, wet chemical methods suffer from drawbacks: 1) The NPs have an organic capping layer on them that inhibits the interaction of the NPs with their environment 2) Available material compositions may be limited, depending on the synthesis technique 3) Processing time is long. The double step LAM process has several advantages over wet chemical methods, as summarized below:

(1) The process is capable of producing bare NPs, even if the starting feedstock material has an organic layer on it. Most organics decompose on laser irradiation at high fluence. Even for organics which might not decompose by laser irradiation, the volume of the organic layer would be much less than the volume of the microparticle, and thus the surface area of the NPs produced much higher than the surface area of the organic. Thus only a negligible fraction of NPs would be covered by the organics, keeping contamination organics to an insignificant level. Bare NPs are necessary for the true realization of NP properties.

(2) The process is capable of producing most metal on oxide NPs as demonstrated in the previous chapters.

(3) Processing time is much shorter for the LAM process (~ 100 g/hr, if all laser power is absorbed) when compared to wet chemical methods.

(4) The technique allows the NPs to be deposited onto substrates or they can be impacted into liquids and stored for future use as a slurry or ink.

Chapter 7: Conclusions

We have demonstrated a method for preparing oxide-metal NPs using a continuous aerosol process. The feasibility of the process was verified using two metals, Au and Ag, and two oxides, TiO_2 and SiO_2. It is likely that the process can be used to produce other combination of NPs as well.

It was shown that the size distribution of the NPs can be tuned using the carrier gas composition. A heavier carrier gas (e.g. Ar) produced larger NPs by constraining the expansion of the laser plume more than the lighter gas (e.g. He). The laser fluence also influenced the particle size distribution by determining the more prominent mechanism for NP formation – shockwave mechanism or evaporative heating mechanism. Higher laser fluence gave a narrower particle size distribution with lower mean particle size. With He carrier gas and a laser fluence of 1.5 J/cm^2, metal NPs with a mean size of about 2 nm were produced on oxide NPs that were about 16 nm.

The titania NPs formed by our process have a broad particle size distribution. A higher breakdown threshold for NP formation of the titania microparticles results in a significant number of NPs being formed via evaporative heating mechanism instead of shockwave mechanism, giving the observed non-uniformity in particle sizes. The coverage of metal on oxide NPs depends on

frequency of the individual drum feeders and the amount of powder in each feeder, and is subject to limited control in the present setup.

The NPs produced by the process are highly charged by photoionization or thermionic emission during the ablation process, and can be thus collected electrostatically. The ionized oxide NPs produced by the process tend to lose their charge by recombining with free electrons in the aerosol and agglomerate. It was demonstrated that it is possible to produce NPs free of agglomeration, provided that they are collected immediately after ablation and before recombination occurs so that the NPs are charged.

Preliminary heating experiments using the electron beam of a TEM were performed to study the size stability of Au NPs to evaluate the potential use as catalysts, which requires that the NP size remains constant. Electron bombardment on TiO_2-Au particles showed peculiar sintering behavior of the Au NPs. A few Au particles readily sintered while others showed an unusual disintering behavior. A few Au NPs readily migrated on the surface of TiO_2, while others appeared to be pinned on the TiO_2 surface. The observations led to the hypothesis that the migration of Au NPs on TiO_2 was dependent of the mode of attachment of Au on TiO_2 – whether they nucleated on TiO_2 or were sticking onto the surface. However, further testing is required to confirm this hypothesis. Electron bombardment also crystallized TiO_2 NPs and also formed amorphous TiO_2-crystalline TiO_2 core-shell NPs.

Chapter 8: Future Work

Sintering behavior of Au NPs on TiO_2 NPs

Preliminary sintering experiments performed *in-situ* on Au NPs using the electron beam in the TEM, showed unusual sintering and migration behavior of Au NPs. A much more controlled experiment using a heating TEM stage, would lead to a better understanding of the observations made in the present work and help design stable Au-TiO_2 catalysts.

Catalytic Activity of Au on TiO_2 NPs

Goodman *et al* [55] have shown significantly enhanced catalytic activity in 1-2 nm gold NPs when they are in contact with a flat titania surface. Au - TiO_2 NPs prepared during the present work have significantly increased surface area compared to the limited surface area of planar substrates which further enhances catalytic activity. We plan to investigate the catalytic activities of these NPs for CO oxidation reactions.

Other Metal on Oxide NP system

Au on Fe_3O_4 is a potential candidate for bio-contrast enhancement agents. We intend to use the double step LAM process for the synthesis of these NPs.

Experimental Apparatus

To produce NPs of more uniform sizes, to effectively control the metal coverage on oxide NPs and to increase production volume and efficiency, it is essential to make a few modifications to the current experimental setup. The following modifications are recommended:

1) A more rigid setup with the more control on the laser focus.

2) A design capable of changing the pressure to give a better control over particle size.

3) An aerosol generator with the capability to control and monitor aerosol density which would provide a control over metal coverage on oxide NPs.

4) A design that would allow a higher laser fluence to ablate the microparticles.

5) A design with shorter collection distances of the charged NPs to obtain non-agglomerated NPs.

References

1 T.V. Choudhary, D.W. Goodman, Topics in Catalysis, 21, 1-3, 25-34 (2003)

2 B. F.G. Johnson, Topics in Catalysis. 24, 1-4, 147-149 (2003)

3 M.V. Rama Krishna, R.A. Friesner, Journal of Chemical Physics 95, 8309 (1991)

4 R. Rossetti, S. Nakahara, L.E. Brus, Journal of Chemical Physics 79, 1086 (1983)

5 W.E Buhro, V.L. Colvin, Nature Materials 2 (3), 138–139 (2003)

6 K. L. Kelly, E. Coronado, L. Zhao, and G.C. Schatz, Journal of Physical Chemistry B 107 (3), 668–677 (2003)

7 G. Raschke, S. Brogl, A. S. Susha, A. L. Rogach, T. A. Klar, and J. Feldmann, Nano Letters 4 (10),1853–1857 (2004)

8 X. Huang , P.K. Jain, I.H. El-Sayed, Nanomedicne 2(5), 681-693, 2007.

9 D.J. Ravnic , Y.Z. Zhang, A. Turhan, A. Tsuda, J.P. Pratt, H.T. Huss, S.J. Mentzer, Microscopy Research and Technique 70(9), 776-781 (2007)

10 Y. Yamamoto, N. Yoshi, H. Shiigi and T. Nagaoka, Solid State Ionics, 177 (26-32) , 2325-2328 (2006)

11 D.C. Castro, T.L. Rodriguez, E.M. Arenas, Z.C. Ortega, M.M. Tanori, Applied Science & Manufacturing, 38(1),107-113 (2007)

12 M. Caglar, S. Ilican, Y. Caglar and F. Yakuphanoglu, Applied Surface Science 255(8), 4491-4496 (2009)

13 Y. Liu, X. Ying and T.Qui, Transactions of Nonferrous Metals Society of China, 16(6), 1370-1373 (2006)

14 V.S. Kalambur, E.K. Longmire, J.C. Bischof, Langmuir, 23 (24), 12329–12336 (2007)

15 V. Ervithayasuporn, Y. Kawakami,Journal of Colloid & Interface Science, 332 (2), 389-393 (2009)

16 W.S. Wang, L. Zhen, C.Y. Xu, W.Z. Shao, Crystal Growth and Design 9 (3): 1558-1568 (2009)

17 C.B. Murray, S.Sun, W.Gascher, H.Doyle, T.A.Betley, C.R.Kagan, IBM Journal of Research and Development, 45(1), (2001)

18 Y. Dimitriev, Y. Ivanova, R. Iordanova, Journal of the University of Chemical Technology and Metallurgy, 43(2),181-192 (2008)

19 Eslamian M, Shekarriz M, Recent Patent in Nanotechnology. 3(2), 99-115 (2009).

20 L.E Shea *et al*., Journal of American Ceramic Society, 79, 3257, 1996

21 J.A. Alonso, *"Structure and properties of atomic nanoclusters"*, Imperial College Press, 2005

22 C. Suryanarayana, Marcel Dekker "*Mechanical Alloying and Milling*", New York 2004, Advanced Materials, 17, 2893-2894 (2005)

23 M.C. Denis, G. Lalande, D. Guay, J.P. Dodelet, R. Schulz, Journal of Applied Electrochemistry, 29(8), (1999)

24 L. Daróczia, D. L. Bekea, G. Posgaya, M. Kis-Vargal, Nanostructured Materials, 6(5-8), 981-984 (1995)

25 Douglas B. Chrisey and Graham K. Hubler, "*Pulsed Laser Deposition of Thin Films*", John Wiley & Sons, 1994

26 H. Oechsner, Applied Physics A: Materials Science & Processing, 8(3) (1975)

27 J.C. Huie *et al.* Smart Materials and Structures. 12. 264-271 (2003)

28 E. Arici, D. Meissner, F.Schaafler, and N.S. Sacriciftci, International Journal of Photoenergy 5, 199-208 (2003)

29 Q. Zhao, L. Houa, R. Huanga, S.Lia, Inorganic Chemistry Communications, 6(12),1459-1462 (2003)

30 V.K. Sergei, A.B. Dawn, A.Tony, X. Lei, Z. Hu, R. Shao, H.F. Jim, Advanced Materials, 16(9-10),795-799 (2004)

31 R.D. Averitt, S.L. Westcott, N.J. Halas, Journal of the Optical Society B, 16(10) (1999)

32 W.Wang, S.A.Asher, Journal of American Chemical Society, 116, 6739-6744 (2004)

33 S. Santra, R.Tapee, J.Dobson, A.Hebard, W.H. Tan, Langmuir 17, 2900-2906, (2001)

34 M. A. Hines P. Guyot-Sionnest, Journal of Physical Chemistry 100, 468-471 (1996)

35 C. Kirchner, Tim Liedl, S.Kudera, T. Pellegrino, A.M. Javier, H.E. Gaub, S. Stölzle, N. Fertig, W.J. Parak, Nano Letters., 5 (2), 331–338 (2005)

36 S. Deka, A. Quarta, M.G. Lupo, A. Falqui, S. Boninelli, C. Giannini, G. Morello, M. De Giorgi, G. Lanzani, C. Spinella, R. Cingolani, T. Pellegrino, L. Manna, Journal of American Chemical Society, 131 (8), 2948–2958 (2003)

37 M. Valden, X. Lai, D. W. Goodman, Science, 281, 1647 (2008).

38 M. S. Chen and D. W. Goodman, Science, 306, 252 (2004);

39 G. C. Bond, D. T. Thompson, Catalytic Review 41, 319 (1999)

40 M.F. Becker, J.R. Brock, and J.W. Keto, "Process for the production of NPs." U.S. Patent No. 5,585,020 (1996)

41 Maciejewski Marek, Fabrizoli Patrizia, Grunwaldt Jan-Dierk, Becker Olav Sven, Baiker Alfons, Physical chemistry chemical physics, 3 (17), 3846-3855, (2001)

42 J. Lee and M.F. Becker, Journal of Applied Physics, 89 (12), (2001)

43 W.T. Nichols, G. Malyavanatham, D.E. Henneke, J.R. Brock, M.F. Becker, J.W. Keto, H.D. Glicksman, Journal of Nanoparticle Research 2, 141 (2000)

44 D. E. Henneke, “Nanoparticles Produced via Laser Ablation of Microparticles”, Dissertation, The University of Texas at Austin, (2001)

45 G. Malyavantham, D.T. O’Brien, M.F. Becker, J.W. Keto, and D. Kovar, Journal of Nanoparticle Research 6 (6), 661-664 (2004)

46 National Institutes of Health (2004), Retrieved Jan 2007 from http://rsbweb.nih.gov/ij/

47 L. Wang, S. Tomura, M. Maeda, F. Ohashi, K. Inukai, and M. Suzuki, Chemistry Letters 1414 (2000)

48 Goutam De, Karamkar B, Journal of Non-Crystalline Solids,272(2-3), 119-126 (2000)

49 W.T. Nichols, G. Malyavanatham, D.E. Henneke, J.R. Brock, M.F. Becker, J.W. Keto, and H.D. Glicksman, Journal of Nanoparticle Research. 2, 141-145 (2000).

50 Y. Chen, R.E. Palmer, and J.P. Wilcoxon, Langmuir, 22 (6), 2851–2855, 2006

51 David Bernard Williams, C. Barry Carter “*Transmission Electron Microscopy”* New York : Plenum Press, 1996

52 Hobbs, L.W., “*Introduction to Analytical Electron Microscopy*” Plenum Press, New York, 1979

53 A. Agrawal, J. Cizeron and V. L. Colvin, Microscopy and Microanalysis, Microscopy and Microanalysis, 4, 269-277 (1998)

54 B.S. Xu, S. Tanaka, Nanostrucured Materials, 6, 727-730 (1995)

55 M.S.Chen and D.W.Goodman, Science 306 (5694), 252-255 (2004)

Vita

Manuj Nahar, son of Narendra Kumar Nahar and Sunita Nahar, was born in Jodhpur, India on November 3rd, 1985. He obtained his Bachelor of Technology in Materials Science and Metallurgical Engineering from Indian Institute of Technlogy Madras, Chennai in June 2007. He started his Master's program in Materials Science and Engineering at the University of Texas at Austin in September 2007.